RESEARCH ARTICLE

Simulation Analysis of Wellhead Sinking during the Development of Weakly Consolidated Marine Hydrate Deposits with Depressurization Strategy

Yanli Wang[1,*] **and Yuanwei Sun**[1]

[1] College of Petroleum Engineering, Shandong Institute of Petroleum and Chemical Technology, Dongying 257061, China

Abstract

Owing to their high calorific value and sustainable characteristics, natural gas hydrates are expected to serve as a promising alternative energy resource to conventional oil and gas in the near future. Of course, this prospect relies on the premise that hydrates can be developed in a safe and efficient manner. Hydrate-bearing sediments are highly sensitive to temperature and pressure conditions and are therefore particularly vulnerable to disturbances induced by production operation, which may result in challenges such as wellhead instability. In this study, the physical parameters of artificially prepared hydrate-bearing sediments were experimentally characterized to provide a parameter foundation for the subsequent simulation-based analysis of wellhead stability. Then, the stability of the wellhead during depressurization-based hydrate development was explored through numerical simulation. Specifically, not only the evolution and underlying mechanisms of wellhead instability were discussed, but also the factors affecting wellhead stability were evaluated. The investigation has demonstrated that the physical properties of hydrate-bearing sediments vary not only with hydrate saturation but also exhibit pronounced stress sensitivity. Furthermore, during the long-term development of hydrate-bearing sediments, the progression of wellhead instability can be divided into three stages, each governed by distinct mechanisms, with the first two stages being predominant. Meanwhile, an increase in pressure-drawdown magnitude combined with a reduction in sediment strength can jeopardize the stability of the wellhead by decreasing the bearing capacity. This study offers technical support and theoretical guidance for the safe and efficient development of weakly consolidated hydrate reservoirs in marine environments.

Keywords: natural gas hydrate, marine hydrate deposits, wellhead instability, depressurization strategy, clean energy.

1 Introduction

The growing global demand for clean energy, combined with the urgent need to transition toward low-carbon alternatives, has spurred intensive

Submitted: 03 January 2026
Accepted: 18 May 2026
Published: 30 May 2026

Vol. 2, **No.** 2, 2026.
10.62762/RS.2026.527395

***Corresponding author:**
✉ Yanli Wang
395497954@qq.com

Citation
Wang, Y., & Sun, Y. (2026). Simulation Analysis of Wellhead Sinking during the Development of Weakly Consolidated Marine Hydrate Deposits with Depressurization Strategy. *Reservoir Science*, 2(2), 203–227.

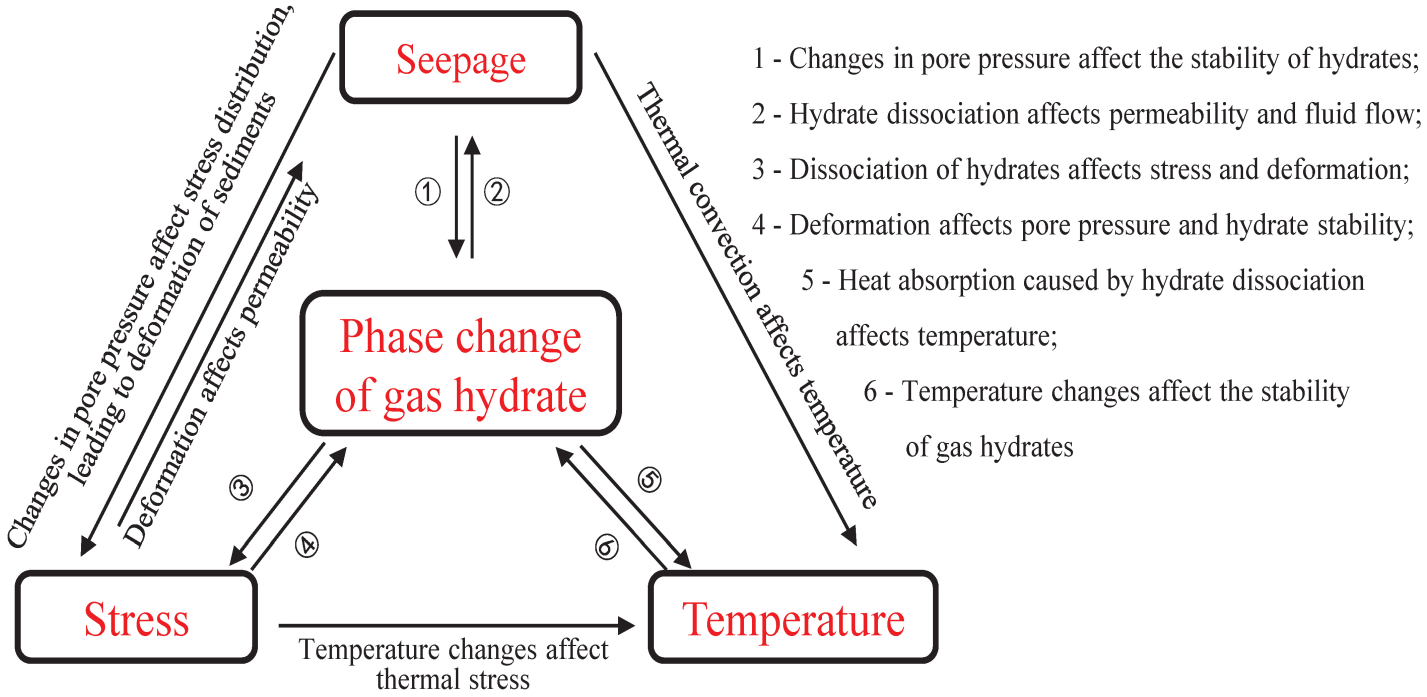

Figure 1. The coupled thermo-hydro-mechanical processes responsible for some geomechanical issues occurs during development of gas hydrate.

research on unconventional oil and gas resources, particularly natural gas hydrates [1–4]. Natural gas hydrates, commonly known as 'combustible ice,' are ice-like crystalline compounds (chemical formula: $CH_4 \cdot nH_2O$) in which methane molecules are trapped within a cage-like lattice of water molecules [5–8]. These resources are predominantly distributed in marine sediments along continental margins at water depths greater than 300 meters, as well as in permafrost regions [9]. In China, natural gas hydrates occur in both marine and permafrost settings, with the former being predominant [10]. The global resource potential is enormous, with conservative estimates suggesting that the volume of methane under standard conditions ranges from 1×10^{15} to 5×10^{15} m^3 [11–13]. More importantly, geological estimates indicate that the total amount of organic carbon stored in global natural gas hydrates is approximately 10^{18} grams [14–16]. This value is about twice the total carbon content of all known conventional fossil fuels, including oil, coal, and natural gas [17]. Consequently, natural gas hydrate is widely regarded as a strategic resource of global importance, with the potential to reshape the future energy landscape [18–20]. Therefore, the successful and sustainable commercial development of marine gas hydrates represents a crucial milestone in securing global energy supply.

The significance of hydrate-bearing sediments lies not only in their potential as an energy resource but also in the environmental risks they entail. As a powerful greenhouse gas, methane released from the destabilization and potential large-scale dissociation of hydrate reservoirs can rapidly enter the ocean and atmosphere, thereby posing a substantial threat to global climate change [21–23]. The vast majority of commercially viable hydrate-bearing deposits occur in weakly consolidated, fine-grained marine sediments, which are generally marked by high porosity and low initial mechanical strength [24–26]. In these sediments, hydrate crystals act as the primary cementing agent, imparting the requisite mechanical strength and stiffness to the sediment.

Among available extraction techniques, depressurization is regarded as the most feasible both technically and economically [27–30]. For most production trials around the world, the strategy of depressurization was commonly used. It operates by lowering the wellbore pressure beneath the hydrate equilibrium, thereby initiating critical but potentially harmful dissociation [31–33]. As solid hydrates dissociate into free gas and water, the geomechanical properties of the reservoir experience fundamental alterations. The loss or weakening of cementation considerably diminishes the structural integrity of porous media, resulting in pronounced reductions in both effective stress and shear strength within the formation [34–36].

At the same time, the dissociation-generated gas leads to a local rise in pore fluid pressure. This complex thermo-hydro-mechanical (THM) coupling mechanism initiates a cascade of effects, including large-scale sediment deformation, potential damage to the sediment skeleton, and serious risks to wellbore integrity [37–39]. Figure 1 presents the coupled thermo-hydro-mechanical processes responsible for these phenomena in hydrate-bearing formations. In weakly consolidated hydrate-bearing sediments, the loss of sediment strength and resulting deformation are especially pronounced.

Although previous research primarily focused on maximizing methane recovery, the structural integrity of the wellbore and wellhead systems has emerged as the principal engineering constraint on sustained production [40, 41]. In conventional oil and gas operations, the wellbore structure—comprising the casing and cement sheath—are primarily engineered to resist static or quasi-static loads. However, during development of gas hydrates, the wellbore experiences complex, highly dynamic loads. Such load combinations include contributions from thermal, hydraulic, and mechanical effects. Among these, the thermal load arises from the endothermic dissociation of hydrates, which causes a temperature drop in the near-wellbore region and induces additional thermal stresses [42]. Furthermore, the hydraulic load, associated with elevated pore pressure, contributes to an increase in circumferential stress within the wellbore region. Finally, the mechanical load primarily consists of compressive and shear stresses acting on the casing–cement system, resulting from the radial deformation of the formation associated with strength reduction. As a consequence, these loads may trigger a range of down-hole failures, including casing deformation, cement failure, and loss of bearing capacity [43]. As these effects extend to the seabed, wellhead instability may occur, presenting as excessive movement, tilting, or structural compromise of surface facilities. The implications of wellhead instability extend beyond production efficiency, posing substantial safety risks such as well control loss, environmental pollution, and catastrophic failure of the production system. In deepwater marine environments, managing and mitigating wellhead instability is extremely challenging and costly, rendering it a critical concern in commercial hydrate exploitation.

Up to now, considerable research has been conducted on wellhead stability during hydrate development, and notable progress has been achieved. To name a few, Guo et al. [44] developed a simple analytical model of wellbore stability that accounts for the saturation-dependent elastoplastic mechanical properties of methane hydrates, establishing a quantitative framework for evaluating the structural integrity of the wellbore system during hydrate production. He et al. [45] investigated the coupled geomechanical responses of both submarine slope stability and wellbore stability during natural gas hydrate drilling and production in slope strata of the South China Sea, highlighting the risks of formation deformation and wellhead displacement under dynamic loading. Cheng et al. [46] investigated the effects of factors, such as layer thickness of hydrate-bearing sediments, initial hydrate saturation, depth of hydrate reservoir, and mudline temperature, on wellhead stability during operation. The investigation results show that operational strategies such as increasing penetration rate and cooling the drilling fluid are effective in mitigating hydrate dissociation around wellbore and enhancing wellhead stability. However, specific quantitative guidelines were not provided [47, 48]. Although informative, the findings of these studies are restricted by some shortcomings. The main limitation is that these studies primarily focus on vertical displacement of wellhead during the hydrate development process, including drilling and gas production.

Inspired by these previous investigations, the following three objectives will be achieved in the present work. Firstly, the evolution of mechanical parameters is investigated through triaxial mechanical experiments. Then, a THM-coupled mathematical model will be developed to simulate the effects of hydrate dissociation on sediment strength and load-bearing capacity. Finally, the effects of major geological parameters on bearing capacity and wellhead displacement were also evaluated.

Based on this, the structure of this study is outlined as follows. In Section 2, triaxial mechanical experiments were carried out using lab-fabricated hydrate-bearing sediment samples, and the mechanical parameters were obtained. In Section 3, the numerical model used for investigation of wellhead instability was developed, and the geometric model was also presented. In Section 4, an in-depth evaluation of the applicability of the mathematical models was carried out. In Section 5, the evolution and mechanisms of wellhead instability were explored.

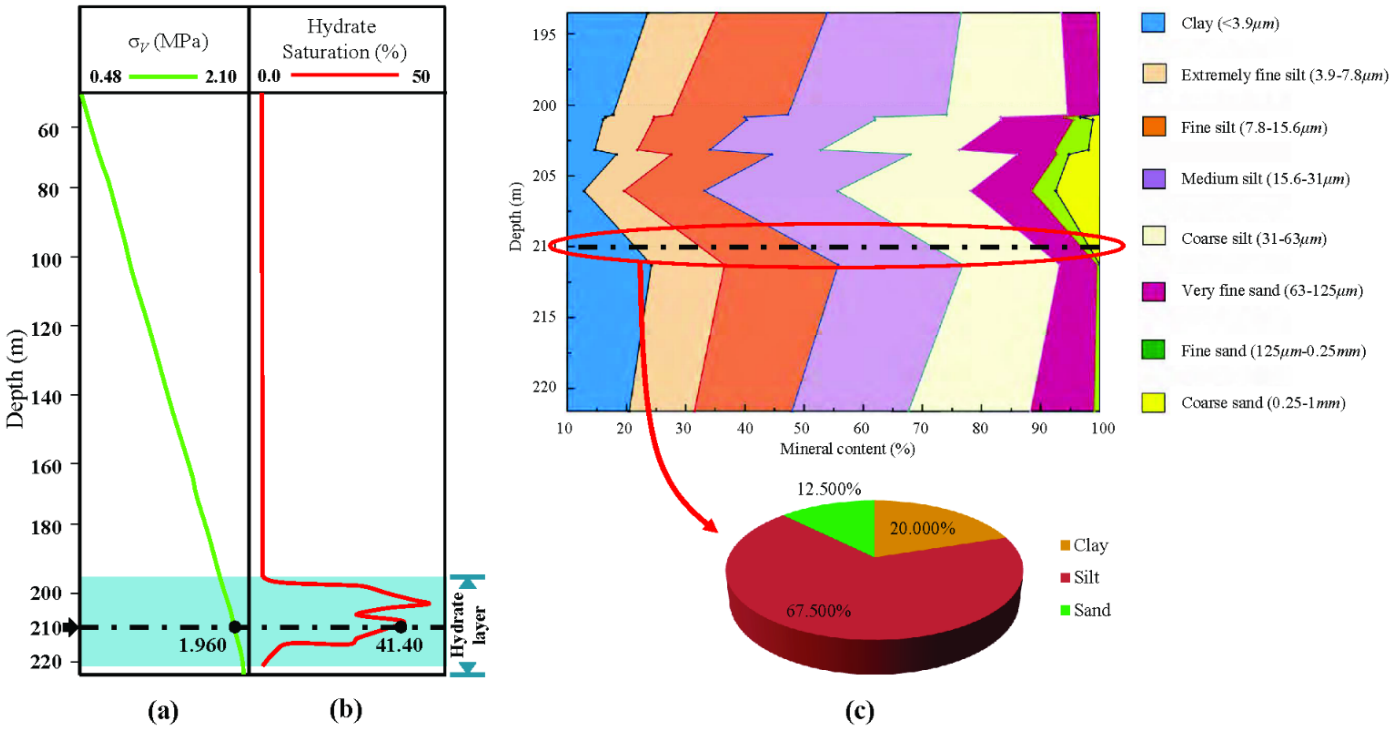

Figure 2. (a) Vertical stress, (b) hydrate saturation, and (c) Mineral composition along the drilling depth in site SH2 of the Shenhu area, northern South China Sea.

2 Experimental study on mechanical parameters of hydrate-bearing sediments

2.1 Experimental materials

Owing to the instability and limited availability of natural hydrate sediments, the experimental samples in this study were prepared artificially [47, 49]. Although the samples were prepared artificially, their composition and preparation conditions were intended to approximate those of natural hydrate-bearing sediments. The study area in the present work is the Shenhu area in the northern South China Sea, and the mineral composition of the prepared hydrate-bearing sediments is based on the SH2 site. Additionally, the hydrate content and applied compressive stress during preparation were designed to reflect the conditions of the hydrate-bearing sediments at this site. Figure 2 presents the relevant information for site SH2 [50–53].

The hydrate layer at site SH2 is located between 195 m and 220 m below the seabed [54]. The characteristics of sediments at 210 m depth were selected as representative values for laboratory sample preparation in this study. As can be seen in Figure 2, the hydrate saturation and effective vertical stress are 41.40% and 1.96 MPa, respectively, at the depth of 210 m below seabed. Additionally, the sediment composition illustrated in Figure 2 comprises 20.0% clay ($< 3.9\,\mu$m), 67.5% fine sand (3.9–63 μm), and 12.5% sand (63 μm–1 mm). Based on this, clay was replaced by bentonite, and silt and sand were substituted with coated sands of different particle sizes in the experiments. Detailed properties of the bentonite and coated sand used in this study are listed in Table 1.

Table 1. Mineralogical composition and fraction of skeleton materials in hydrate-bearing samples.

Materials	Particle size/mesh	Weight percentage/%	Substitute minerals
Bentonite	–	20.0	Clay
Coated sand	2000	20.0	Fine silt
	600	30.0	Medium-coarse silt
	100	17.5	Fine sand
	50	12.5	Medium-coarse sand

Methane (CH_4) constitutes the main component of gas released during hydrate dissociation, accounting for up to 96% by volume. Accordingly, CH_4 was employed as the guest gas in the preparation of hydrate-bearing sediments, and it was purchased from Chongqing Yuchuang Gas Co., LTD, and the purity is 99.9%. The water used in experiment is deionized water.

2.2 Experimental system and method

The experimental apparatus employed in this study facilitates both the artificial synthesis of

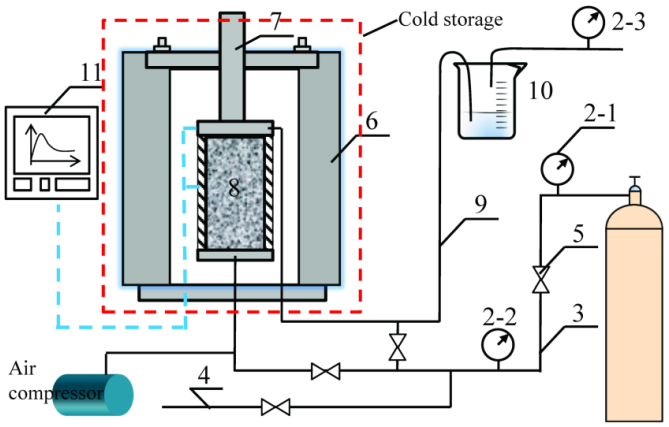

Figure 3. The experimental system.

hydrate-bearing sediments and mechanical testing, and the spatial layout diagram is shown in Figure 3. As observed in Figure 3, the experimental system is composed of a gas supply module, a pressure control module, a cold storage, a triaxial testing apparatus, and a data acquisition module. The main component of the gas supply module is a methane cylinder that supplies the gas required for the formation of methane hydrates in sediment. The methane cylinder has a capacity of 30 L and an initial pressure of 7 MPa. During the preparation of hydrate-bearing sediment samples, the pressure in cylinder gradually decreases, which may lead to instability in the pressure within the autoclave. Therefore, an air compressor, which serves as the main component of the pressure control module, is employed to maintain a constant pressure throughout the experiment. The cold storage provides and maintains a low-temperature environment that promotes the formation and stability of hydrate deposits, with a minimum operating temperature of $-30\,^{\circ}\mathrm{C}$. The autoclave, a cylindrical pressure vessel used to contain the prepared samples, is capable of withstanding pressures as high as 100 MPa. In addition, the primary components of the data acquisition module include temperature sensors (accuracy $\pm 0.1\,^{\circ}\mathrm{C}$), pressure sensors (accuracy ± 20 kPa), and strain gauges (accuracy ± 0.01 mm).

The experiment is primarily divided into two stages: the preparation of samples and the subsequent mechanical experiments. The detailed experimental method is as follows:

(1) **Preparation of samples.** Initially, bentonite and coated sand with different particle sizes were introduced into the high-pressure reactor in proportions specified in Table 1. Then, deionized water with a mass of m_w was measured according to the formula shown in Equation (1) and added to the autoclave. At this stage, the temperature of the cold storage was adjusted to $0\,^{\circ}\mathrm{C}$ and maintained during the preparation operation. Afterwards, sufficient amount of methane was continuously introduced into the autoclave for a period of 24 hours.

After the formation of hydrate-bearing sediment, it was placed into the sample mold, and a pressure of approximately 2.0 MPa was applied using an axial piston [55].

$$m_w = \frac{207}{239} V \varphi S_h \rho_h \tag{1}$$

where V is the sample volume, φ is the porosity, S_h is hydrate saturation, and ρ_h is hydrate density.

(2) **Mechanical experiments.** Once an adequate number of samples had been prepared, the cylindrical samples were positioned on a triaxial testing machine. Then, the rock sample, enclosed in thermoplastic tubing, was subjected to confining pressure through hydraulic oil, and axial load was applied using an axial piston in a controlled displacement manner. Notably, the axial load should be maintained continuously until the rock sample reached failure [56]. Throughout the experiment, measurements of stress, strain, temperature, pressure, and related parameters were continuously recorded and stored.

2.3 Experimental results

It is crucial to establish a physical property parameter model based on experimental results for analyzing and evaluating wellhead stability during the development of hydrate-bearing sediments [57]. In conventional parameter-determination models, the physical properties of hydrate-bearing sediments are typically characterized as functions of hydrate saturation alone [58–60]. Through the experiments conducted with the setup shown in Figure 3, effects of effective confining pressure, and hydrate saturation on physical parameters of hydrate-bearing sediments were determined. The methodological framework of this experimental investigation is divided into two sequential phases. Firstly, based on the experimental results at varying hydrate saturation, a function was fitted and obtained using the hydrate saturation S_h as the governing variable. Then, based on this, the model can be further improved by combining experimental results of the synergistic effect of confining pressure. In

this study, six hydrate saturation values were selected at intervals of 0.15, ranging from 0 to 0.75, namely 0, 0.15, 0.30, 0.45, 0.60, and 0.75. Correspondingly, the effective confining pressure (P_c) was designed as the following six levels: 0 MPa, 5 MPa, 10 MPa, 15 MPa, 20 MPa, and 25 MPa.

2.3.1 Elastic parameters

Figure 4 presents the variation curves of the elastic modulus and Poisson's ratio of hydrate-bearing sediments as functions of hydrate saturation and confining pressure. As can be seen in Figure 4(a), the elastic modulus increases markedly with increasing hydrate saturation. For the hydrate-free sediment, the elastic modulus is 713.6 MPa. Afterwards, the elastic modulus exhibits a linear increase with rising hydrate saturation in the sediment. When the hydrate saturation reaches 0.75, the experimentally measured elastic modulus attains a value of 1894.1 MPa. For the purpose of facilitating related numerical simulations, a functional relationship between the elastic modulus of hydrate-bearing and hydrate saturation was fitted as

$$E(S_h) = 1503.5S_h + 675.03 \quad R^2 = 0.9691 \tag{2}$$

where S_h is hydrate saturation.

From Figure 4(a), it is indicated that the Poisson's ratio is also significantly influenced by hydrate saturation. For the hydrate-free sediments, the Poisson's ratio is 0.320. However, as the pore space was increasingly filled with hydrate, the Poisson's ratio exhibits a continuous decreasing trend. When the hydrate saturation reaches 0.75, the Poisson's ratio decreases to 0.283, representing a reduction of approximately 11.56% compared to the hydrate-free case. This behavior is primarily attributed to the presence of the hydrate in sediments, which enhances the deformation resistance. In previous studies, the Poisson's ratio of hydrate-bearing sediments was often assumed to be constant, which may result in overestimated simulation outcomes [61]. To facilitate numerical simulations of geomechanical issues such as wellhead stability, a quadratic function, as presented in Equation (3), was fitted to capture the influence of hydrate saturation on the Poisson's ratio.

$$v(S_h) = 0.0452(S_h)^2 + 0.0804S_h + 0.3188 \quad R^2 = 0.9902 \tag{3}$$

As illustrated in Figure 4(b), the confining pressure applied during the experiment significantly affects the elastic modulus of hydrate-bearing sediments. With increasing applied confining pressure, the elastic modulus rises significantly. When the confining pressure applied during the experiment increases from 0 MPa to 25 MPa, the elastic modulus rises nonlinearly from 781.9 MPa to 1352.3 MPa. To accurately update the elastic modulus of hydrate-bearing sediments in subsequent numerical simulations, a quadratic equation, as presented in Equation (4), was fitted to characterize the influence of confining pressure on the elastic modulus.

$$E(P_c) = 0.4884(P_c)^2 + 34.795P_c + 792.13 \quad R^2 = 0.9738 \tag{4}$$

To derive an equation that simultaneously accounts for the effects of confining pressure and hydrate saturation, the relationship between hydrate saturation and elastic modulus was first normalized, as follows:

$$E(S_h)_0 = 1 + 2.227S_h \tag{5}$$

By combining Equations (4) and (5), a comprehensive equation for determining the elastic modulus of hydrate-bearing sediments was obtained, accounting for the combined effects of confining pressure and hydrate saturation.

$$\begin{aligned} E(P_c, S_h) =& (1 + 2.227S_h)(0.4884(P_c)^2 \\ &+ 34.795P_c + 792.13) \end{aligned} \tag{6}$$

Furthermore, the Poisson's ratio of hydrate-bearing sediments is substantially influenced by confining pressure. As illustrated in the right subfigure Figure 4(b), the Poisson's ratio decreases markedly with increasing confining pressure. During the experimental increase of confining pressure from 0 MPa to 25 MPa, the Poisson's ratio of the rock sample decreases from 0.293 to 0.253, representing a reduction of up to 13.65%. To quantify the influence of confining pressure on the Poisson's ratio, the experimental results were fitted, resulting in the quadratic function presented in the following equation.

$$v(P_c) = 0.00004(P_c)^2 - 0.0026P_c + 0.2936 \quad R^2 = 0.9846 \tag{7}$$

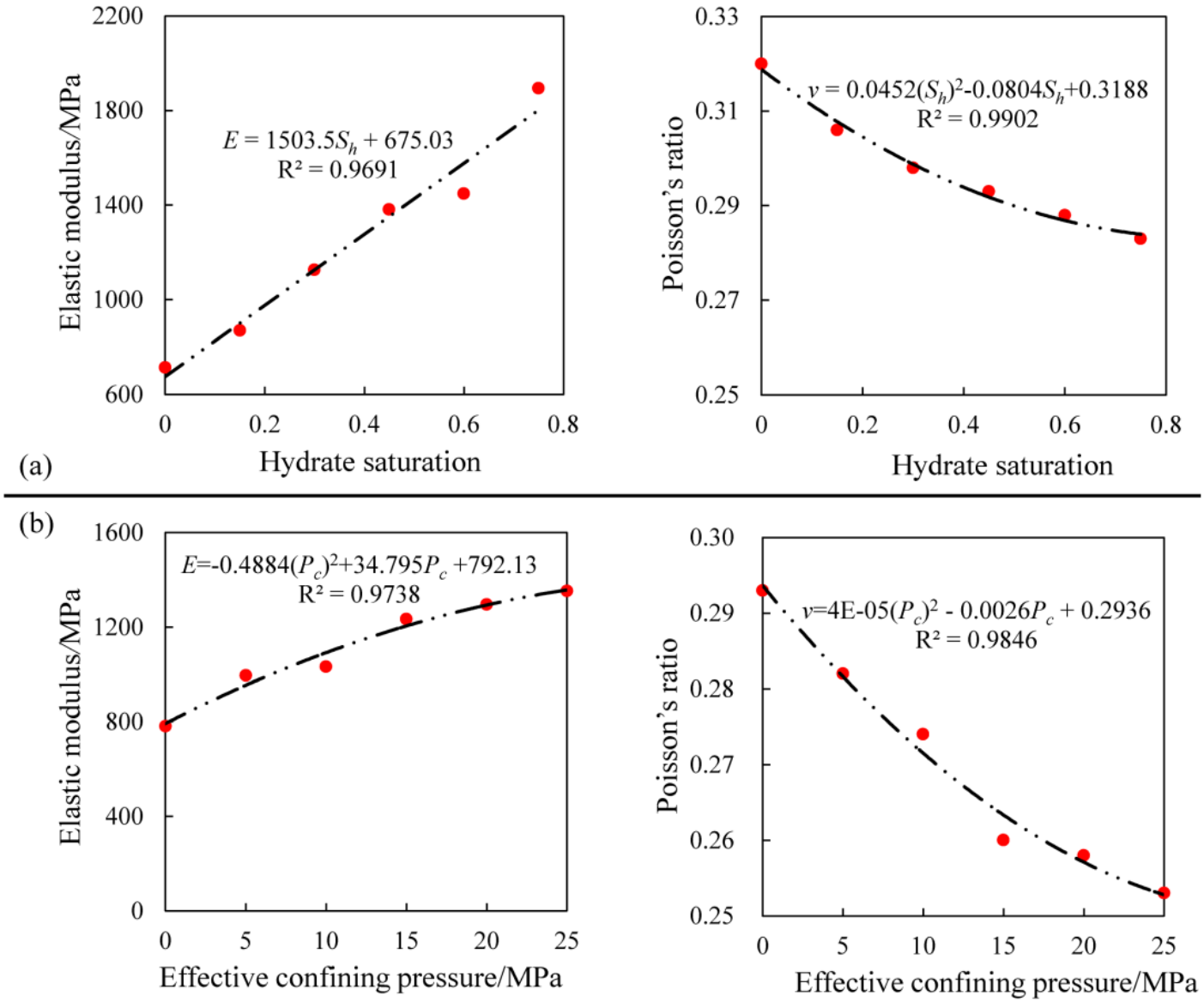

Figure 4. Experimental results of elastic parameters. (a) Effect of hydrate saturation, (b) Effect of confining pressure.

Similarly, by combining the normalized Equations (3) and (7), a Poisson's ratio determination equation is obtained that comprehensively considers the combined effects of confining pressure and hydrate saturation, as follows:

$$v(P_c, S_h) = (0.1418(S_h)^2 + 0.2522S_h + 1)(0.00004(P_c)^2 - 0.0026P_c + 0.2936) \quad (8)$$

In the simulation of wellhead stability, the elastic properties of hydrate-bearing sediments can be updated using the USDFLD subroutine based on Equations (6) and (8) in ABAQUS 2016 software.

2.3.2 *Strength parameters*

Hydrate saturation and confining pressure exert profound influences not only on the elastic modulus and Poisson's ratio of hydrate-bearing sediments but also on the strength parameters [62, 63]. Therefore, the experiment explored the effects of these two factors on the cohesion and internal friction angle of hydrate-bearing sediments, and the results were shown in Figure 5.

As shown in the left subgraph of Figure 5(a), variations in hydrate saturation in hydrate-bearing sediments can obviously affect the cohesion. An increase in hydrate saturation strengthens the bonding or cementation between particles, resulting in an approximately linear increase in sediment cohesion. In the absence of gas hydrates, the sediment exhibits weak cementation,

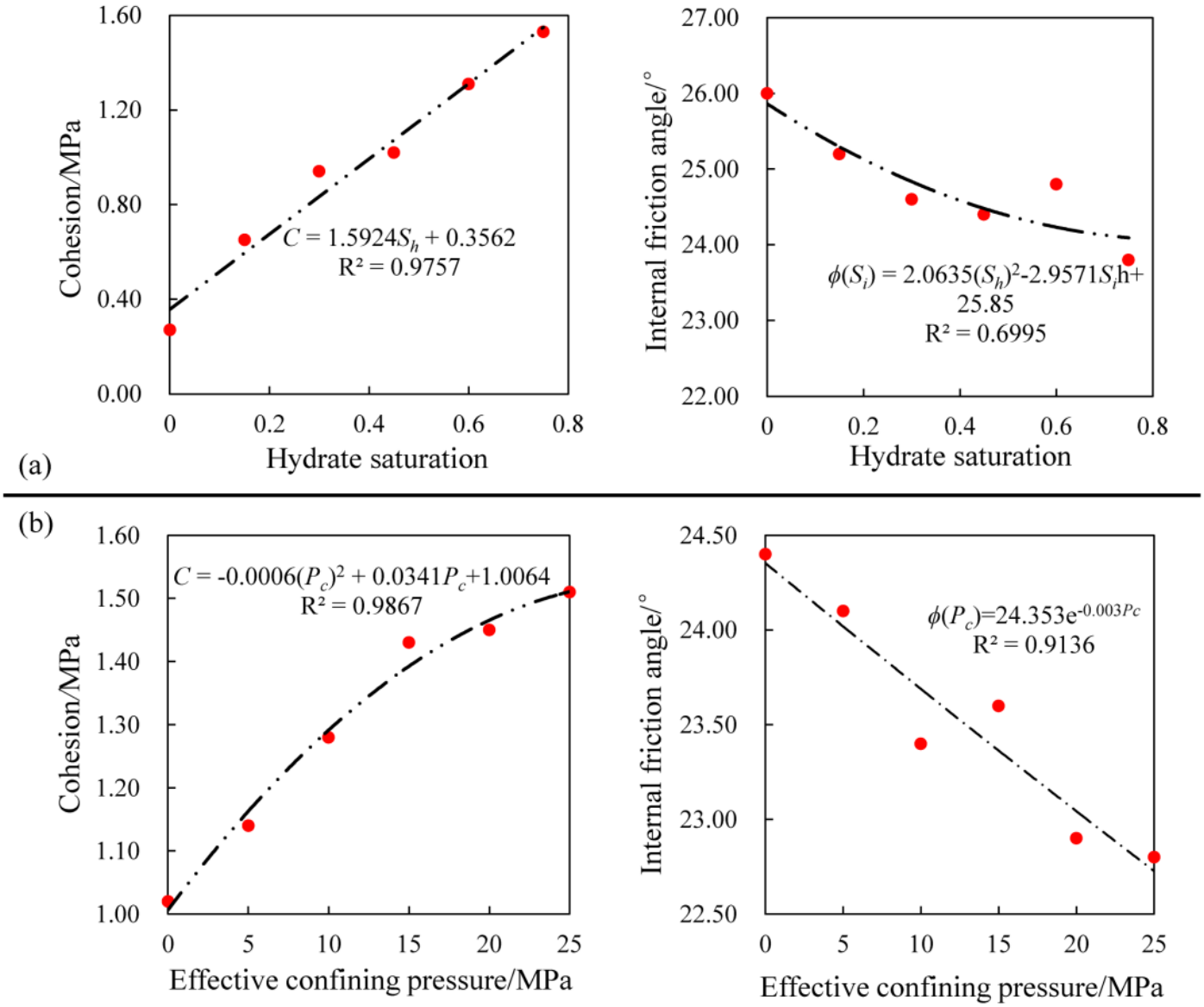

Figure 5. Experimental results of strength parameters. (a) Effect of hydrate saturation, (b) Effect of confining pressure.

with a cohesion of only 0.27 MPa. At a hydrate saturation of 0.75, the resulting cohesion is quantified at 1.53 MPa, representing a 4.47-fold increase relative to the hydrate-free state. By fitting the experimental results, a linear equation was derived, as shown below, to describe the relationship between the cohesion of hydrate-bearing sediments and hydrate saturation.

$$C(S_h) = 0.3562 + 1.5924S_h \tag{9}$$

However, as shown in the right subgraph of Figure 5(a), the internal friction angle gradually decreases with the formation of gas hydrates in the sediment (i.e., with increasing hydrate saturation). At low hydrate saturation, particle contacts within the sediment are primarily supported by the soil matrix, and hydrates, acting merely as filler, do not substantially influence inter-particle friction. In this case, the sediment exhibits a high internal friction angle. In this study, when there is no hydrate, the internal friction angle is 26.2°. As hydrate saturation increases, hydrates progressively occupy the pore spaces between particles, diminishing direct particle-to-particle contact and thereby substantially reducing inter-particle friction. The internal friction angle of the hydrate-bearing sediments decreases to 23.8° when hydrate saturation reaches 0.75. It can be inferred that with further increases in hydrate saturation, the internal friction angle will continue to decrease. This is because, at very high hydrate saturation, sediment particles become almost completely separated by hydrates [64, 65]. Since it remains necessary to assign the internal friction angle in wellhead stability simulations, the effect of hydrate

saturation on the internal friction angle is expressed by the following equation.

$$\phi(S_h) = 25.85 + 2.0635(S_h)^2 - 2.9571S_h \quad R^2 = 0.6995 \tag{10}$$

The increase in confining pressure in experiment enhances the compaction and bonding among the skeleton particles, thereby increasing the strength. As shown in the left subgraph of Figure 5(b), the cohesion of hydrate-bearing sediment increases with confining pressure, following a quadratic relationship. The cohesion is only 1.02 MPa when the confining pressure is 0. However, the cohesion attains 1.51 MPa when the confining pressure is raised to 25 MPa, which is about 48.04% higher than that measured under the zero-confining-pressure condition. This is because the increase in confining pressure enhances the compaction between particles, thereby strengthening the cementing effect of the cementing material to the skeleton particles [66, 67]. However, the pressure-melting mechanism under high confining pressure partially mitigates this enhancement, which is evidenced by a reduction in the slope of the curve shown in the graph. The experimental results were well fitted using the following equation.

$$\begin{aligned} C(S_h, P_c) =& 0.3562\left(-0.0006(P_c)^2 + 0.0341P_c\right. \\ &\left. +1.0064\right)(1 + 4.47S_h) \end{aligned} \tag{11}$$

Meanwhile, as shown in the right subgraph of Figure 5(b), the internal friction angle exhibits a modest decreasing trend as confining pressure increases. At low confining pressure, sliding between the skeleton particles primarily depends on inter-particle contact and the cementation provided by hydrates. The "bonding" of hydrates objects on particles will significantly enhance frictional resistance. When the confining pressure is 5.0 MPa, the internal friction angle is $24.1°$. As the confining pressure increases, the interaction between hydrates and skeleton particles is dominated by compression, stability of hydrates is destroyed. Then, particle sliding is nearly eliminated, and the internal friction angle stabilizes at a low level. When the confining pressure in experiment is 20 MPa and 25 MPa, the internal friction angles of the hydrate-bearing sediments decrease to $22.9°$ and $22.8°$, respectively. To quantitatively characterize the relationship between internal friction angle and confining pressure, the experimental results shown in Figure 5(b) were fitted to the exponential function form as:

$$\phi(P_c) = 24.353e^{-0.003P_c} \quad R^2 = 0.9136 \tag{12}$$

To incorporate the combined effects of hydrate saturation and confining pressure, Equations (10) and (12) were integrated to derive the following relationship:

$$\begin{aligned} \phi(P_c, S_h) =& 24.353e^{-0.003P_c} \cdot \left(25.85 + 0.0798(S_h)^2\right. \\ &\left. -0.1144S_h\right) \end{aligned} \tag{13}$$

2.3.3 *Seepage-related characteristic parameters*

Hydrate saturation also significantly affects the permeability and porosity of hydrate-bearing sediments, primarily through the formation, distribution, and pore-space occupation of hydrates within the sediment [68–70]. Figure 6 presents the experimental results illustrating the effects of hydrate saturation and confining pressure on the permeability and porosity of hydrate-bearing sediments.

As shown in the Figure 6(a), the permeability decreases significantly with increasing hydrate saturation. In the absence of hydrates, the sediment exhibits favorable physical properties, with a high permeability of 11.6 mD, and the effective porosity is as high as 38.6%. However, as hydrate saturation increases, hydrates progressively occupy the pore spaces within sediments. Due to the immobility of hydrates, the flow channels of water and gas in the pores can be blocked, thereby substantially reducing permeability [71]. When the hydrate saturation increases to 0.75, the permeability of the hydrate-bearing sediments decreases sharply to 0.78 mD, accompanied by a reduction in porosity to 11.6%. It can be predicted that if the hydrate saturation continues to increase, the sediment permeability will approach zero, and its porosity will further decline. By fitting the experimental results of the effects of hydrate saturation on permeability and porosity in Figure 6(a), the functional forms given in Equation (14) and (15) are obtained.

$$K(S_h) = 11.6\left(1 - S_h\right)^{1.971} \quad R^2 = 0.8436 \tag{14}$$

$$\begin{aligned} \Phi(S_h) &= -18.81\left(S_h\right)^2 - 21.988S_h + 38.675 \\ R^2 &= 0.9873 \end{aligned} \tag{15}$$

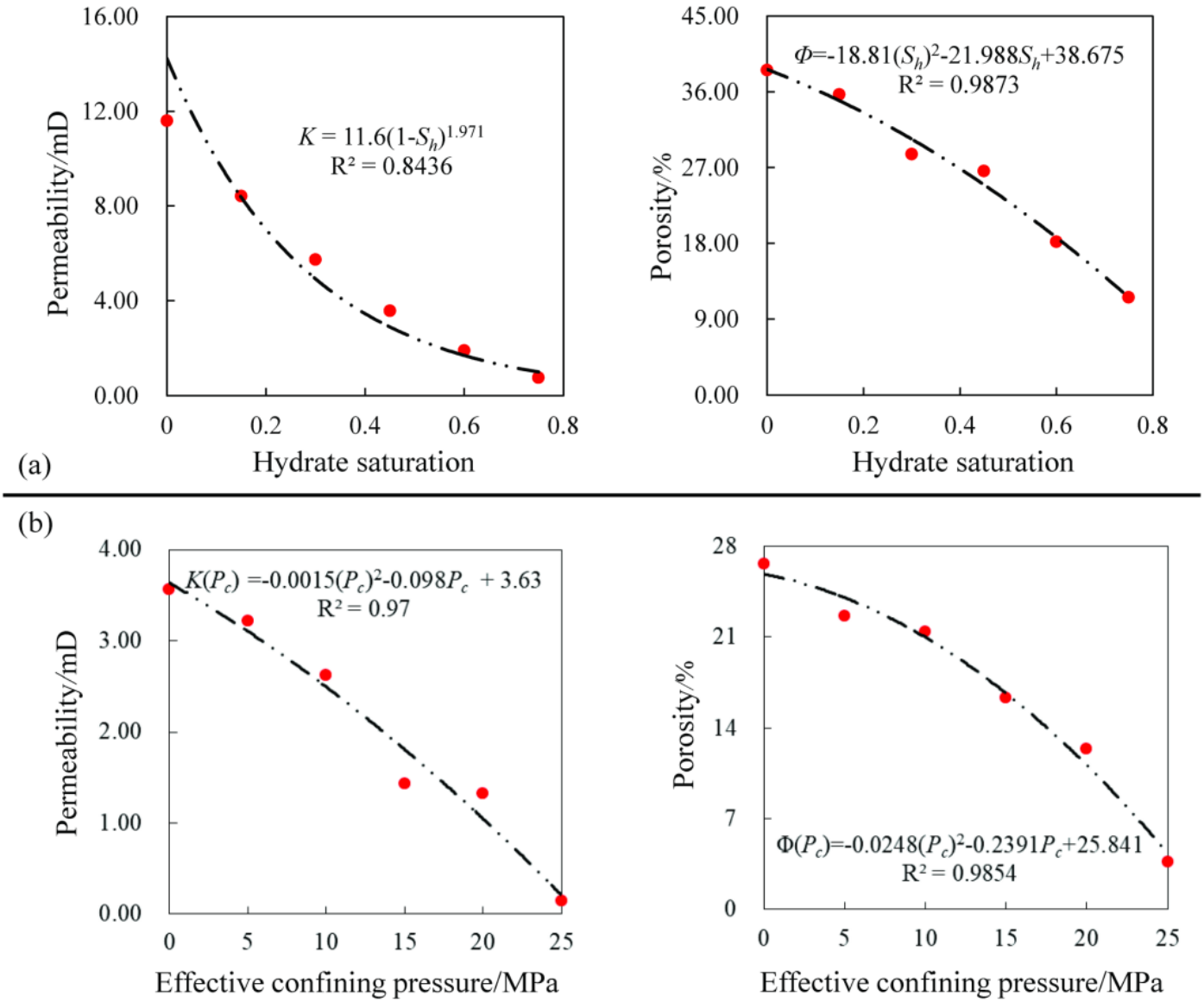

Figure 6. Experimental results of seepage-related characteristic parameters. (a) Effect of hydrate saturation, (b) Effect of confining pressure.

The effect of confining pressure on the porosity and permeability of hydrate-bearing sediments is primarily governed by the induced volumetric strain on the sediment, leading to a significant alteration in the internal pore structure. As demonstrated in Figure 6(b), higher confining pressure leads to progressive compression of the pore space within hydrate-bearing sediments. This results in narrower fluid-flow pathways, increased flow resistance, and a pronounced reduction in permeability. During the increase of confining pressure from 0 MPa to 25 MPa, the permeability decreases from 3.57 mD to 0.15 mD, representing a reduction of up to 95.80%. In other words, as the confining pressure increases, the permeability of hydrate-bearing sediments will be reduced to an almost negligible level. The variations of permeability and porosity with confining pressure exhibit similar trends, with the porosity decreasing to 3.64% at a confining pressure of 25 MPa. Based on the experimental results shown in Figure 6(b), the variations of permeability and porosity with confining pressure can be fitted as follows:

$$K(P_c) = -0.0015\,(P_c)^2 - 0.098P_c + 3.63 \quad R^2 = 0.97 \tag{16}$$

$$\Phi(P_c) = -0.0248\,(P_c)^2 - 0.239P_c + 25.841 \quad R^2 = 0.9854 \tag{17}$$

By applying the methodology outlined in Sections

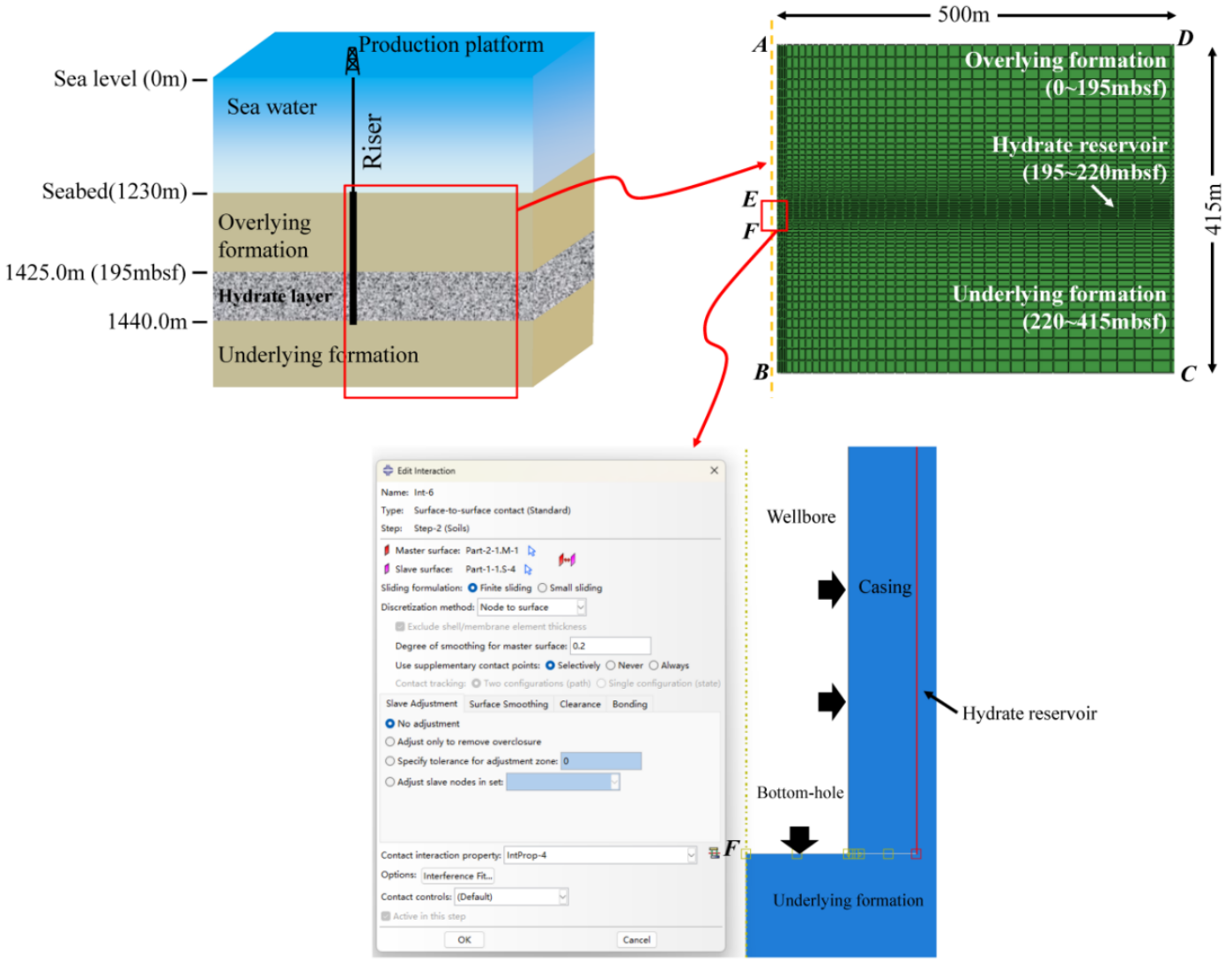

Figure 7. Geometric model.

2.3.1 and 2.3.2, the permeability and porosity of hydrate-bearing sediments are fitted and expressed as Equations (18) and (19), respectively.

$$K(P_c) = -0.0015(P_c)^2 - 0.098P_c + 3.63 \quad R^2 = 0.97 \tag{18}$$

$$\Phi(P_c) = -0.0248(P_c)^2 - 0.239P_c + 25.841 \quad R^2 = 0.9854 \tag{19}$$

In simulation, the physical parameters of the sediment can be updated in real time according to Equations (6), (8), (11), (13), (18), and (19) by obtaining hydrate saturation and stress of each element.

3 Numerical model and implementation method

In this study, a thermo–hydro–mechanical–chemical (T-H-M-C) coupling model was developed to accurately characterize the multi-physics interactions governing wellhead stability during the depressurization-based development of marine gas hydrates. The model is fully integrated with the governing equations of mass, energy, and momentum conservation, as well as the phase change dynamics of hydrates in the reservoir. In addition, the complex interface mechanics between the wellbore system and weakly consolidated formations need to be considered in the model [72–74]. A complete description of the multi-physics coupling theory used in this study can be found in previous publication [50] and is not duplicated herein.

In the present work, all simulation investigations

are based on the following main assumptions. (1) The sediments in the same formation depth are homogeneous and isotropic. (2) The only fluid that can flow in sediment is gas and water, and hydrates cannot flow. (3) Within the pore space of the reservoir, fluid motion is governed by Darcy's law. (4) The effects of thermal stress were neglected in the simulation. (5) The density, specific heat capacity, and thermal conductivity of both hydrates and sedimentary rock are assumed to remain constant. (6) The lateral load acting on the wellhead is neglected, and only the vertical load is taken into account in this study. (7) The interaction between the casing and the cement is disregarded, and the two components are combined into a single part termed the wellhead. (8) No external energy was supplied during the simulation, and the changes in sediment temperature were entirely induced by hydrate dissociation.

3.1 Geometric model

In this study, Site SH2 in the Shenhu area of the South China Sea is selected as a representative example, and the corresponding geometric model is developed as shown in Figure 7. As illustrated in Figure 7, the investigation model is composed of two primary components or parts: the wellhead system and the sediment. Although a fully 3D model provides greater geometric realism, the structural symmetry of both components allows the problem to be simplified. Therefore, to enhance computational efficiency, a 2D axisymmetric model is adopted [75].

At Site SH2, a hydrate layer with a thickness of 25 m is situated at a depth of 195 m beneath the seabed [76, 77]. Consequently, the sediment part depicted in Figure 7 has a total thickness of 415 m, with the hydrate layer positioned at mid-depth. To minimize the influence of the wellbore and outer boundaries on the simulation results, the lateral extent of the hydrate reservoir is set to 500 m. In practice, phase change of gas hydrates and wellhead instabilities predominantly occur in the near-wellbore region and within the hydrate layer. There, mesh refinement was applied to these two areas in the model. In total, the sediment component is discretized into 25,600 CAX4P elements. The wellhead system is modeled using a uniform casing ($13^{3/8}$ inches), neglecting variations in wellbore diameter across different drilling stages. The wellhead system is meshed with uniform element size and discretized into 92 CAX4R elements. The depth of the wellhead is aligned with that of the wellbore, with its base positioned 20 meters below the lower boundary of the hydrate layer. In other words, both the wellbore depth and the length of the wellhead system are 240 m.

In the simulation, two sequential analysis steps are performed: first, the Geostatic step, followed by the wellhead instability analysis. In the Geostatic step, the wellhead system is deactivated with the "Model Change" function [78, 79]. This procedure allows the determination of the sediment's initial state. In the second analysis step, the "Model Change" function is re-used to activate the wellhead system, enabling its participation in the simulation of wellhead instability.

Appropriate contact settings are essential for accurately simulating the interaction between the wellhead and the surrounding sediment. In this study, the interaction between the wellhead system and the sediment was modeled as surface-to-surface contact. This contact condition needs to be applied to both the lateral and bottom surfaces of the casing in simulation.

3.2 Implementation of hydrate dissociation and dynamic updating of physical parameters

The ABAQUS 2016 platform offers strong capabilities for nonlinear solid-mechanics calculations; however, it does not include built-in functions for hydrate dissociation. In the present work, this missing capability was realized by developing two user-defined subroutines. Specifically, the DISSOCIATION subroutine implements hydrate dissociation, while the USDFLD subroutine handles the time-dependent evolution and updating of the sediment's physical parameters. The implementation framework of the two subroutines is shown in Figure 8.

As can be seen in Figure 8(a), hydrate dissociation is modeled based on the dissociation kinetics of methane hydrate, and the hydrate saturation determined using the following equation (i.e., Equation (20)) [80–82]. In this subroutine, the change in saturation during each time increment is compared with the initial value to ensure that the resulting values remain within a reasonable range [83].

$$\frac{dS_h}{dt} = \frac{K_{rd}}{\rho_h} M_h A_{dec} S_h (\phi_e P_e - \phi_g P_g) \qquad (20)$$

As can be seen in Figure 8(b), the update of sediment physical properties is performed via the USDFLD subroutine, which is driven by the outputs of the DISSOCIATION subroutine. When using ABAQUS 2016 for modeling, two field variables must be defined, corresponding to hydrate saturation and

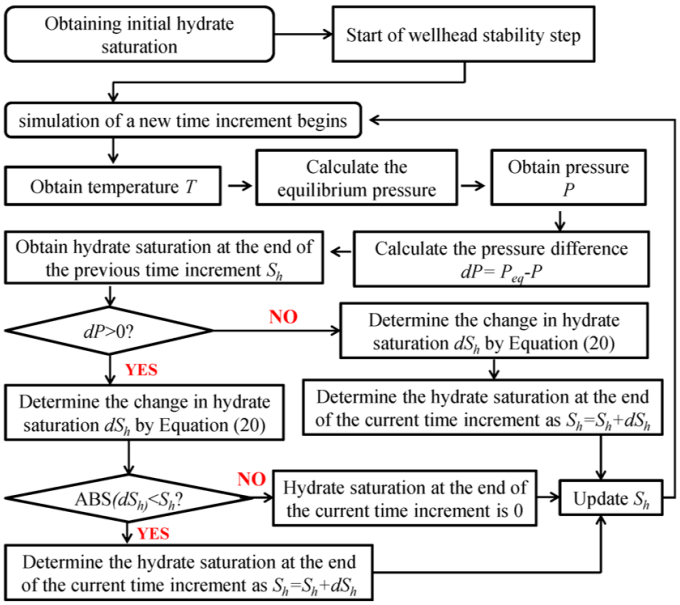

(a) DISSOCIATION subroutine for hydrate dissociation

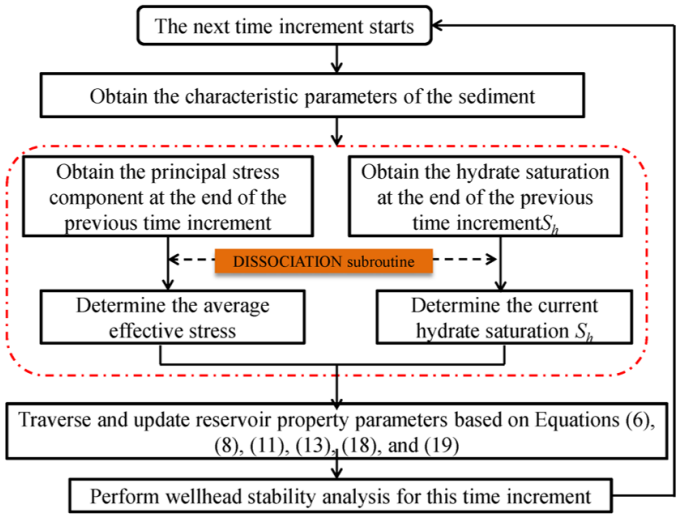

(b) USDFLD subroutine for updating physical prameters

Figure 8. Implementation framework of the two subroutines.

effective stress, respectively [84]. The relationship between the physical parameters and the field variables—hydrate saturation and effective stress—is defined in accordance with Equations (6), (8), (11), (13), (18), and (19). At the end of each time increment, the subroutine obtains the hydrate saturation and stress for each element or node and updates the corresponding physical parameters of the sediment. In this way, simulation in the next time increment is performed based on the updated sediment properties.

3.3 Boundary conditions, initial conditions and loads

(1) Boundary conditions

Boundary AD: Since boundary AD functions as a free boundary, no mechanical boundary conditions need to be specified along this boundary. However, in the simulation, both its temperature and pressure are assumed to remain constant, corresponding to the seawater temperature and pressure at the seabed respectively.

Boundary BC and CD: Only displacement boundary conditions are applied to these two boundaries, with the normal component of displacement being constrained.

Boundary BF: This boundary is a symmetry boundary and is therefore assigned symmetric boundary conditions.

Boundary EF: This boundary corresponds to the hydrate layer, where the temperature is set to the bottom-hole temperature, and the pressure is maintained at the bottom-hole production pressure during the simulation.

(2) Initial conditions

The simulation requires defining four initial conditions—in-situ stresses, hydrate saturation, temperature, and pore pressure—all of which are imposed on the sediment part, not on the wellhead system.

(3) Loads

Boundary AD: An external pressure load, with a magnitude corresponding to the seabed pressure, is imposed on this boundary.

4 Applicability verification

4.1 Applicability verification

The highlights of this work are the implementation of hydrate dissociation, and the simulation of formation subsidence and wellhead instability. In this section, the applicability of the proposed methodology was verified through comparisons of hydrate dissociation and sediment deformation against findings from two relevant previous investigations. In the course of verification, the simulation was conducted under the same conditions and with the same parameters as in the previous investigations.

Figure 9 illustrates the verification model and the results of the comparative analysis. Figures 9(a) and

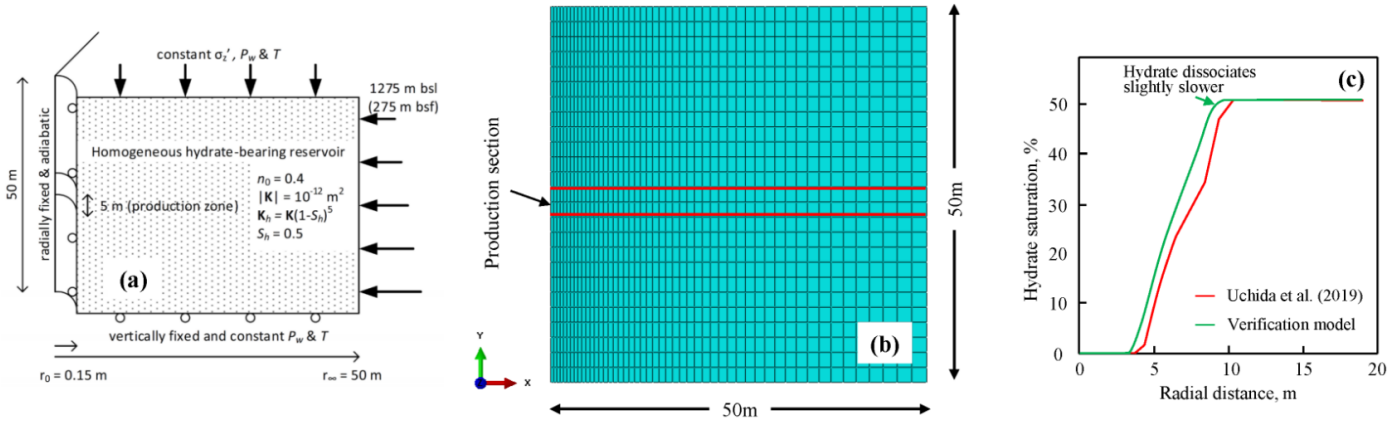

Figure 9. Verification of function of hydrate dissociation. (a) Model geometry of used by Uchida et al. [78]; (b) Model used for verification; (c) The comparison results of final hydrate saturation distribution.

b depict the model employed in Uchida's study of hydrate development and that used for verification in the present work, respectively. Figure 9(c) presents a comparison of the simulation results derived from two models. As can be seen in Figure 9(c), the research outcomes generated by the two models demonstrate strong consistency. This confirms the applicability of the numerical model and the implementation approach employed herein for the precise simulation of hydrate development operations. Nonetheless, a divergence is observed in Figure 9(c), where the hydrate dissociation rate derived from this study is notably lower than that reported by Uchida et al. [78]. The primary reason is that the model employed herein accounts for the stress sensitivity of the hydrate-bearing sediments. This yields lower sediment permeability, leading to a deceleration in the processes of both seepage and thermal diffusion.

Figure 10 shows the verification result of the investigation method proposed in the present work based on the comparison based on seabed subsidence. The case study depicted in Figure 10 investigates sediment subsidence during the development of gas hydrates using horizontal wellbore and depressurization strategies. As observed in Figure 10(b), although slight differences exist between the results obtained by the research method proposed in this study and those reported in previous studies, the differences remain minimal. This indicates that the method proposed in this study is suitable and reliable for analyzing geomechanical processes associated with hydrate development.

At the same time, the feasibility of the research method was verified by comparing the simulated triaxial mechanical parameters with some experimental results in the second section. The comparison results

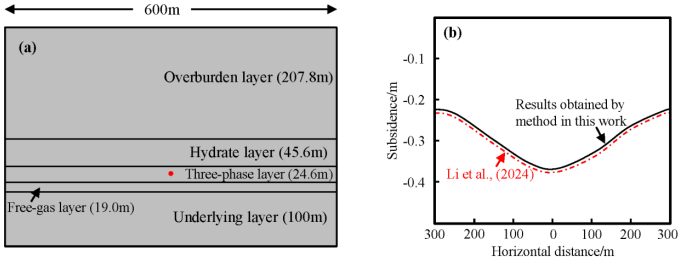

Figure 10. Verification of function of seabed subsidence. (a) Model geometry of used by Li et al. [79]; (b) The verification results.

Table 2. Comparison of experimental or simulation results (take the cohesion as example).

Confining pressure	Simulation value, MPa	Experimental value, MPa	Error, %
5 MPa	1.10	1.15	4.55
10 MPa	1.27	1.26	0.79
15 MPa	1.40	1.43	2.14
20 MPa	1.48	1.45	2.03

were displayed in Table 2. As can be seen in Table 2, the difference between the two data is extremely small, and the maximum error is only 4.55%. For the experimental results under other experimental conditions, the comparative results are also similar to this. The negligible error further demonstrates that the experimental value and simulation model used in this study are suitable for conducting relevant simulations of wellhead stability.

4.2 Grid independence analysis

An appropriate element density can effectively balance simulation efficiency and simulation accuracy. For this purpose, a grid independence analysis was conducted on the simulation model. In the present

work, 12800, 25,600, 38400 and 51200 elements were meshed to optimize the grid configuration in geometric model. As can be seen from Table 3, a decrease in element size leads to a longer simulation time. Moreover, this effect becomes increasingly pronounced as the element becomes denser. However, the cumulative gas production initially increases and then gradually stabilizes when the grid becomes denser. The number of elements corresponding to the transition point of this trend is exactly 25,600. Therefore, selecting an element configuration corresponding to 25,600 elements is considered reasonable. Nevertheless, further increasing the number of elements would significantly prolong the simulation time and reduce computational efficiency, while providing little improvement in computational accuracy.

Table 3. Results of grid independence analysis.

Number of elements	**Simulation time, min**	**Accumulated gas production, $10^7 m^3$**
12800	12.52	1.24
25600	19.47	1.36
38400	29.22	1.37
51200	41.27	1.37

4.3 Basic data used for simulation

The simulation data used in this study were derived from two main sources. The first source was publicly available geological and engineering data from site SH2 in the Shenhu area of the South China Sea [85]. The second source was the set of physical property models established in Section 2. By integrating a range of exploration findings for the site, the data presented in Figure 11 was consolidated. It should be emphasized that Figure 11 lacks parameter information for the underlying sediment. Therefore, the parameters of the underlying sediment were assigned using the properties of sediment at a depth of 220 m. Meanwhile, the sediment properties in the model are heterogeneous in the depth direction. Moreover, Table 4 lists the other physical properties and principal engineering parameters.

4.4 Evolution and mechanism of wellhead instability

Throughout the development process, hydrate dissociation compromises the mechanical integrity and bearing capacity of the sediments, thereby promoting wellhead instability [93, 94]. Therefore, Figure 12 illustrates the evolution of hydrate

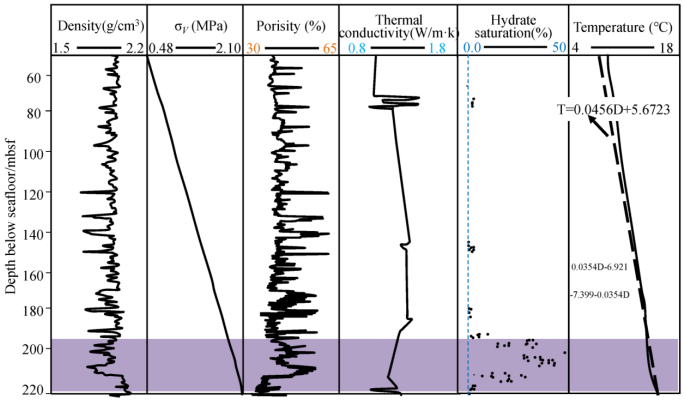

Figure 11. The profiles of some characteristic parameters of sediment in the model [86–92].

dissociation, the bearing capacity, and wellhead sinking during hydrate production.

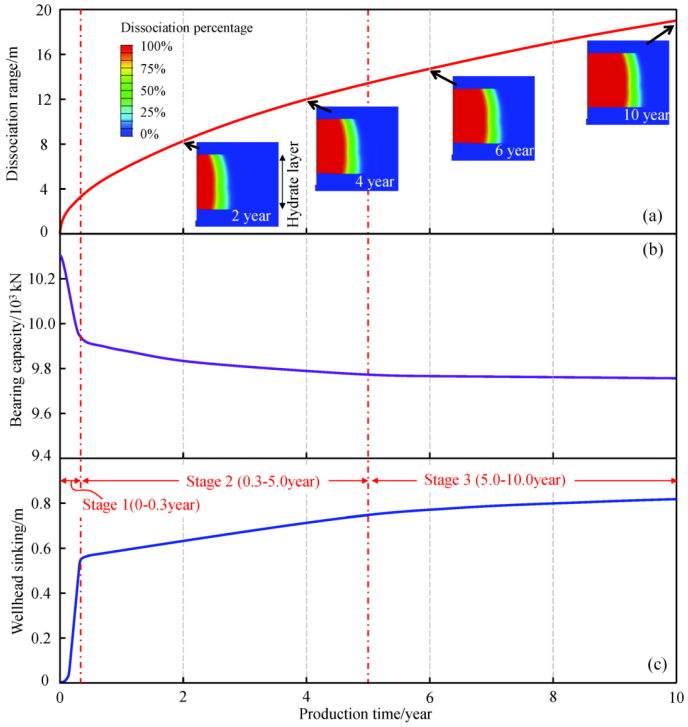

Figure 12. Evolution of hydrate dissociation, bearing capacity, and wellhead sinking during hydrate production. (a) Dissociation range, (b) Bearing capacity, (c) wellhead sinking.

As can be seen in Figure 12, with the progression of production operation, the vertical displacement of wellhead casing increases continuously, whereas the vertical bearing capacity exhibits a gradual decline. Furthermore, the evolution of bearing capacity is opposite to that of wellhead sinking. Nevertheless, the governing mechanisms influencing bearing capacity and wellhead sinking differ across the various stages of hydrate development. From the start of the development operation to approximately 0.3 year,

Table 4. Other basic data for simulation of wellhead stability.

Parameters	Value	Unit
Elastic modulus	Determined by Equations (6)	MPa
Poisson's ratio	Determined by Equations (8)	–
Cohesion	Determined by Equations (11)	MPa
Internal friction angle	Determined by Equations (13)	°
Permeability	Determined by Equations (18)	mD
Porosity	Determined by Equations (19)	–
Biot's coefficient	0.85	–
Pore pressure	$(P_{\text{seal}} + \rho g H)/10^6$	MPa
Specific heat	2000	J/(kg.K)
Well depth	240	m
Casing size	$13\frac{3}{8}$	Inches
Total production cycle	10.0	Year
Depressurization amplitude	6.0	MPa

the wellhead stability is severely threatened, and its sinking increases sharply. At 0.3 year, the wellhead sinking had increased to 0.56 m. The primary reason is that the bearing capacity of the wellbore supporting the wellhead system decreases rapidly during this stage. During this stage, the bearing capacity rapidly decreased from 10.3×10^3 kN to 9.92×10^3 kN. The change in bearing capacity during this stage can also be attributed to the rapid dissociation of gas hydrates around wellbore. Before hydrates begin to dissociate, the adhesive bonding of sediment around effectively supports the wellhead system (see Figure 13(a)). Owing to development operation-related disturbances, such as depressurization, hydrate dissociation causes a rapid weakening of this adhesive bonding and a significant decrease in supporting force [95]. At this time, the support provided by the sediment to the wellhead system primarily arises from the upward frictional resistance generated under compressive stress. Even though the hydrate dissociation range near the wellbore is limited within this stage, it is enough to modify the support mechanism provided by the adjacent sediments to the wellhead system.

After 0.3 year of hydrate production, a noticeable deceleration in the wellhead sinking rate is observed. More precisely, during the next 4.7 years (i.e., between 0.3 and 5.0 year), the wellhead system undergoes continued subsidence, though at a minimal rate. Over these 4.7 years, the wellhead sinking rose from 0.56 m to 0.76 m, with an average rate of increase of merely 0.043 m/year. The wellhead experiences this sinking largely as a consequence of the depressurization strategy, which has caused an overall reduction in pore pressure within the model. The decrease in pore pressure causes the sediment pores to compress under increasing effective stress, resulting in sediment subsidence [96]. Consequently, the wellhead system sinks along with the sediment. Even with a 10.4 m extension of the hydrate dissociation region, the resulting influence on sediment subsidence and wellhead sinking is minor. Simultaneously, the bearing capacity experienced a minor reduction of 140 kN, which was mainly attributed to change of external extrusion on casing resulting from changes in pore pressure and stress in this process.

After 5 years of continuous development, the pore pressure within the investigation model has largely stabilized. From then on, the sustained depressurization strategy no longer induces notable changes in pore pressure and sediment stress. Therefore, the bearing capacity and wellhead sinking curves exhibit marginal variations at this stage. Over these five years, the wellhead has exhibited a negligible sinking of 0.21 m, concomitant with a modest reduction in bearing capacity of 50 kN. These minor changes are primarily attributed to the dissociation region of the approximately 6.4-m-wide hydrate during this stage, which induces mild compaction of the surrounding sediment.

4.5 Effect of depressurization amplitude on wellhead stability

As demonstrated in Section 5.2, wellhead instability was mainly induced by hydrate dissociation during the early stage of production. In addition, the overall reduction in sediment pore pressure caused by depressurization further contributes to the downward sinking of the wellhead. Therefore, depressurization

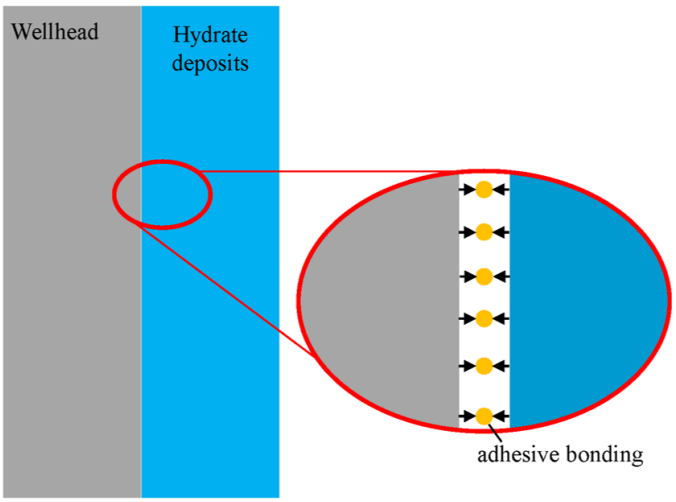

(a) before hydrate dissociation

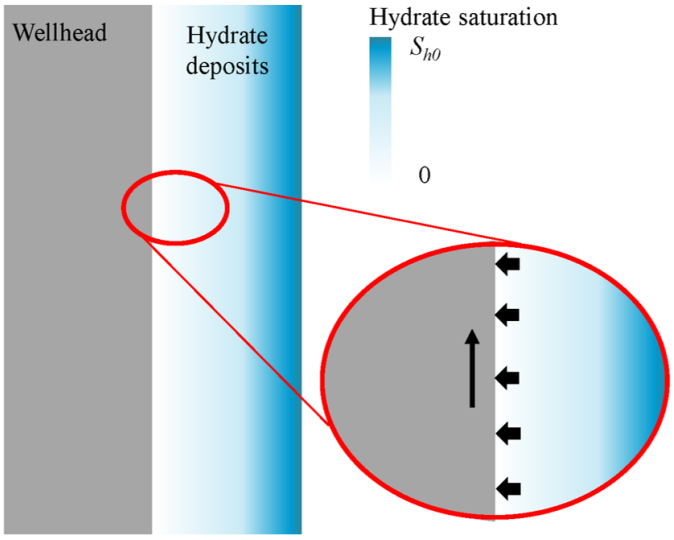

(b) at 0.3years of hydrate development

Figure 13. Evolution of support mechanism at the sediment–wellhead interface in the initial phase of hydrate production.

amplitude is also an important factor affecting wellhead stability [97, 98]. In this section, the effect of depressurization amplitude on wellhead stability was investigated, and the investigation results were shown in Figure 14. In this study, four depressurization levels were considered, with amplitudes of 2.0 MPa, 4.0 MPa, 6.0 MPa, and 8.0 MPa respectively, and other parameters are presented in Table 2. It is worth noting that this design is reasonable, as the maximum depressurization amplitude achieved during Japan's trial production in the Nankai Trough is as high as 10 MPa [99].

As can be seen in Figure 14, the amplitude of depressurization exerts a pronounced influence on wellhead stability. When the depressurization amplitude is 2.0 MPa, the wellhead undergoes a sinking of 0.62 m over the 10-year development period. However, as the depressurization amplitude increased to 4.0 MPa, 6.0 MPa, and 8.0 MPa, the resulting wellhead sinking increased correspondingly to 0.69 m, 0.81 m, and 0.93 m respectively. In fact, the variation in wellhead sinking observed under different depressurization amplitudes primarily results from the impact of the development operation on the pore pressure of sediments in model. This is because, on the one hand, the results indicate that the hydrate dissociation throughout the simulation period is nearly identical for all applied depressurization amplitudes (see Figure 14(a)). The final dissociation ranges of hydrates under four different depressurization amplitudes are 18.10 m, 18.44 m, 18.80 m, and 19.38 m, respectively. In this way, the mechanism of sediment subsidence arising from differences in the hydrate dissociation is excluded. On the other hand, during the early stage of development, hydrate dissociation around the well causes the sediment bonding effect supporting the wellhead system to fail, leading to similar subsidence among the four cases [100]. Across the four depressurization amplitudes, this mechanism leads to a wellhead sinking of 0.53(10) m. Regardless of the depressurization amplitude, after approximately 5 years of development, the pore pressure throughout the entire model becomes fully disturbed and subsequently stabilizes. For high depressurization amplitudes, pore pressure within the model becomes naturally low, resulting in more severe compaction and subsidence of deposits under the load of the overlying formation. The bearing capacity also decreases correspondingly at this stage (see Figure 14(b)). Then, the wellhead system exhibits pronounced sinking accompanied by sediment compaction.

At present, there is no unified criterion for determining wellhead instability. In the present work, a sinking of 0.75 m for the wellhead system is adopted as the threshold for defining instability. Therefore, for vertical-well hydrate production via depressurization, the depressurization amplitude should be controlled to less than 6.0 MPa to ensure that the wellhead system remains stable.

5 Effect of elastic modulus of hydrate-free sediments

Sediment compaction and subsidence induced during the development process constitute major contributors

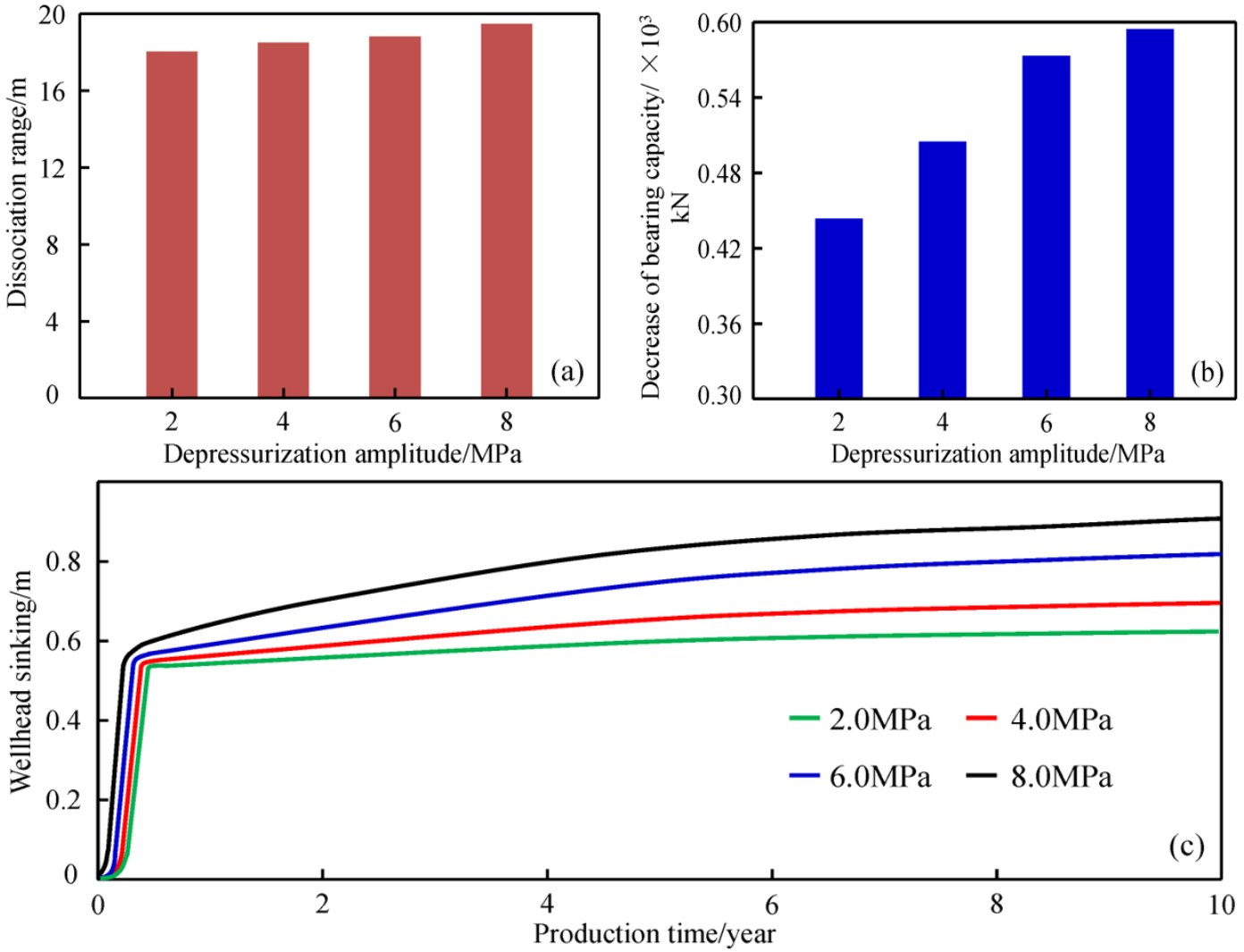

Figure 14. Effect of depressurization amplitude on wellhead stability. (a) hydrate dissociation; (b) bearing capacity; (c) wellhead sinking.

to pronounced wellhead sinking [101, 102]. Therefore, the inherent strength of hydrate-free sediment also plays an important role. In this section, the effect of hydrate-free sediment elastic modulus on wellhead instability was investigated, with values set at 400 MPa, 600MPa, 800MPa, and 1000MPa respectively, and the investigation results were presented in Figure 15.

In general, sediments characterized by a low elastic modulus also exhibit diminished strength and correspondingly limited resistance to deformation [103]. In depressurization-driven development processes, the dissociation of gas hydrates and attendant decline in pore pressure engender pronounced compression of pores and throats within the sediment, resulting in a low permeability (see Figure 15(d)). In this way, fluid flow and heat transfer in this sediment are naturally weaker. The dissociation range of gas hydrates around the wellbore is naturally narrow. As depicted in Figure 15(a), at an elastic modulus of merely 400 MPa, the dissociation radius of gas hydrates within the near-wellbore region extends only to 14.18 m. Even upon elevating the elastic modulus to 600 MPa, the dissociation radius extends only to 16.14 m. Nonetheless, the difference in the dissociation range of gas hydrates has little effect on the bonding effect between the wellhead system and surrounding sediments. If any impact occurs, it is manifested primarily as a minor disturbance to the stability of sediments around wellbore. The effect of variations in sediment elastic modulus on wellhead stability is primarily manifested through their influence on sediment subsidence or deformation. Owing to the low overall elastic modulus of sediments within model, the pressure reduction associated with depressurization operation induces an anomalously pronounced subsidence of sediments in model [104, 105]. The

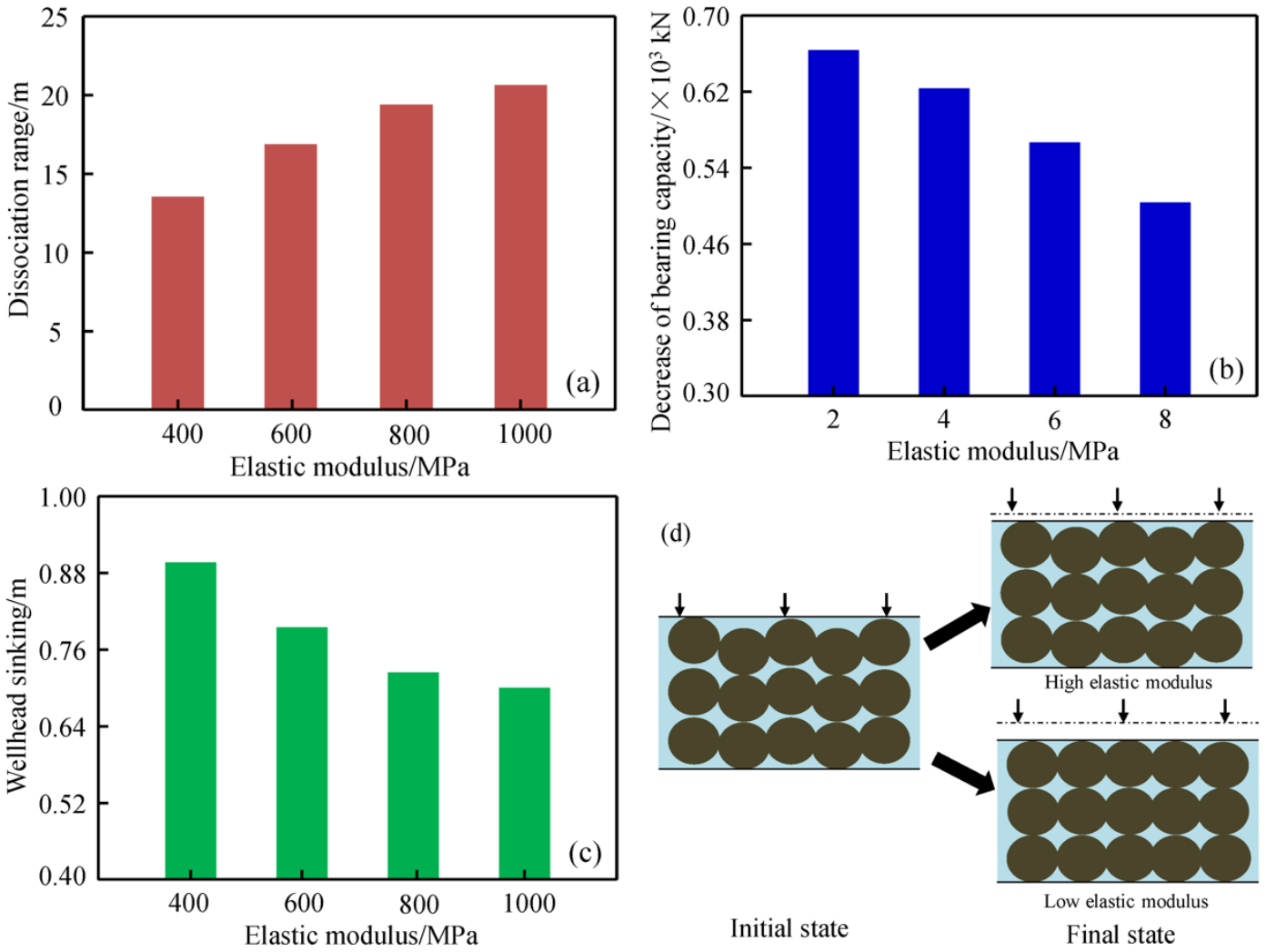

Figure 15. Effect of elastic modulus of hydrate-free sediments on wellhead stability. (a) hydrate dissociation; (b) bearing capacity; (c) wellhead sinking; (d) Compaction at the particle scale.

bearing capacity undergoes a pronounced decline in development process, the stability of the wellhead system is markedly reduced, and the wellhead consequently experiences rapid sinking. From Figure 15(b) and Figure 15(c), it can be clearly see that when the elastic modulus of hydrate-free sediment is 400 MPa, the reduction in bearing capacity and wellhead sinking are 0.66×10^3 kN and 0.90 m respectively.

As the elastic modulus increases, although the hydrate dissociation region expands, the reduction in bearing capacity becomes less pronounced. This is because a higher sediment skeleton strength effectively inhibits the closure of pores and throats, thereby maintaining high heat transfer and fluid seepage (see Figure 15(d)). Compared to the low elastic modulus, the elevated bearing capacity associated with a higher elastic modulus contributes to improved stability of the wellhead system. As shown in Figure 15(c), when the elastic modulus of hydrate-free sediment increases to 1000 MPa, the resulting wellhead subsidence is limited to only 0.68 m. This sinking value is 24.44% lower than that corresponding to an elastic modulus of 400 MPa. If the threshold mentioned above remains applicable, when the elastic modulus of hydrate-free sediment is below 600 MPa, the depressurization magnitude must be appropriately reduced to ensure wellhead stability.

6 Conclusions and future works

The main conclusions obtained in the present work are as follows:

(1) The physical properties of hydrate-bearing sediments are influenced not only by hydrate saturation but also by the prevailing stress (or confining pressure) conditions. Moreover, although the mechanisms through which hydrate saturation and effective confining pressure influence the physical

properties of hydrate-bearing sediments differ, their overall trends are largely consistent. The influence of hydrate saturation arises from the filling of sediment pores, whereas the effect of effective confining pressure is exerted through its control on skeleton deformation. As hydrate saturation or confining pressure increases, all physical parameters decrease except for the elastic modulus and cohesion increase, while Poisson's ratio, internal friction angle, permeability, and porosity decrease.

(2) The progression of wellhead sinking can be divided into three stages: a rapid sinking stage, a continuous sinking stage, and a decelerated sinking stage. The primary cause of the rapid wellhead sinking in the first stage is the swift dissociation of hydrates, which undermines the bonding between the sediment and casing, leading to a pronounced reduction in bearing capacity. The sinking of the wellhead in the latter two stages is primarily attributed to sediment compaction and subsidence induced by depressurization, which reduces the bearing capacity.

(3) Regardless of the development cases, the wellhead sinking observed during the initial stage of long-term production operation is largely consistent. This is governed by the dominant controlling mechanism responsible for wellhead subsidence during this stage. During this stage, the wellhead system will undergo subsidence as long as hydrate dissociation occurs within a certain range around wellbore.

(4) During hydrate production, although an increase in the depressurization magnitude does not markedly influence hydrate dissociation, it can substantially reduce the sediment's bearing capacity on the wellhead system, thereby threatening wellhead stability. When the depressurization magnitude increased from 2.0 MPa to 8.0 MPa, the wellhead subsidence grew from 0.62 m to 0.93 m. Moreover, if the threshold for identifying or evaluating wellhead instability is assumed as 0.75 m, the depressurization magnitude must remain below 6.0 MPa. The influence mechanism of sediment elastic modulus on wellhead instability is primarily manifested through its control over sediment deformation and subsidence within the development processes. The stability of the wellhead system improves as the elastic modulus of the sediment increases.

This study presents only a preliminary numerical investigation into the effects of wellhead subsidence during marine hydrate production. Further in-depth investigations are required to ensure the safe and efficient long-term development of gas hydrates. Accordingly, the subsequent research agenda is outlined as follows.

(1) The lateral loads acting on the wellhead during the development process were not considered in this study, yet they constitute an important factor influencing the stability of the wellhead system.

(2) In this study, the simulation was conducted using a vertical wellbore as a representative example. However, horizontal wellbores are more commonly employed in hydrate production. In future work, stability analyses of the wellhead during hydrate development should be performed using horizontal well configurations. Moreover, depressurization represents only one of the commonly employed strategies for hydrate development. The stability analysis of wellhead system under alternative hydrate production strategies should also be taken into consideration.

Data Availability Statement

Data will be made available on request.

Funding

This work was supported without any funding.

Conflicts of Interest

The authors declare no conflicts of interest.

AI Use Statement

The authors declare that no generative AI was used in the preparation of this manuscript.

Ethical Approval and Consent to Participate

Not applicable.

References

[1] Zhao, X., Geng, Q., Zhang, Z., Qiu, Z., Fang, Q., Wang, Z., ... & Li, Y. (2023). Phase change material microcapsules for smart temperature regulation of drilling fluids for gas hydrate reservoirs. *Energy, 263*, 125715. [CrossRef]

[2] Li, Q., & Wu, J. (2022). Factors affecting the lower limit of the safe mud weight window for drilling operation in hydrate-bearing sediments in the Northern South China Sea. *Geomechanics and Geophysics for Geo-Energy and Geo-Resources, 8*(2), 82. [CrossRef]

[3] Boswell, R., & Collett, T. S. (2011). Current perspectives on gas hydrate resources. *Energy & environmental science, 4*(4), 1206-1215. [CrossRef]

[4] Chong, Z. R., Yang, S. H. B., Babu, P., Linga, P., & Li, X. S. (2016). Review of natural gas hydrates as an energy resource: Prospects and challenges. *Applied energy, 162*, 1633-1652. [CrossRef]

[5] Ruppel, C. D., & Waite, W. F. (2020). Timescales and processes of methane hydrate formation and breakdown, with application to geologic systems. *Journal of Geophysical Research: Solid Earth, 125*(8), e2018JB016459. [CrossRef]

[6] Li, J. F., Ye, J. L., Qin, X. W., Qiu, H. J., Wu, N. Y., Lu, H. L., ... & Kou, B. B. (2018). The first offshore natural gas hydrate production test in South China Sea. *China geology, 1*(1), 5-16. [CrossRef]

[7] Ye, J. L., Qin, X. W., Xie, W. W., Lu, H. L., Ma, B. J., Qiu, H. J., ... & Bian, H. (2020). The second natural gas hydrate production test in the South China Sea. *China Geology, 3*(2), 197-209. [CrossRef]

[8] Moridis, G. J., Collett, T. S., Boswell, R., Kurihara, M., Reagan, M. T., Koh, C., & Sloan, E. D. (2009). Toward production from gas hydrates: current status, assessment of resources, and simulation-based evaluation of technology and potential. *SPE Reservoir Evaluation & Engineering, 12*(05), 745-771. [CrossRef]

[9] Boswell, R., Collett, T. S., Frye, M., Shedd, W., McConnell, D. R., & Shelander, D. (2012). Subsurface gas hydrates in the northern Gulf of Mexico. *Marine and Petroleum Geology, 34*(1), 4-30. [CrossRef]

[10] Wang, H., Yang, S., Wu, N., Zhang, G., Liang, J., & Chen, D. (2013). Controlling factors for gas hydrate occurrence in Shenhu area on the northern slope of the South China Sea. *Science China Earth Sciences, 56*(4), 513-520. [CrossRef]

[11] Archer, D., Buffett, B., & Brovkin, V. (2009). Ocean methane hydrates as a slow tipping point in the global carbon cycle. *Proceedings of the National Academy of Sciences, 106*(49), 20596-20601. [CrossRef]

[12] Milkov, A. V., & Sassen, R. (2002). Economic geology of offshore gas hydrate accumulations and provinces. *Marine and Petroleum geology, 19*(1), 1-11. [CrossRef]

[13] Sloan Jr, E. D., & Koh, C. A. (2007). *Clathrate hydrates of natural gases*. CRC press.

[14] Max, M. D., & Johnson, A. H. (2020). *Exploration and Production of Oceanic Natural Gas Hydrate Critical Factors for Commercialization*. Evaluation. [CrossRef]

[15] Ruppel, C. D., & Kessler, J. D. (2017). The interaction of climate change and methane hydrates. *Reviews of Geophysics, 55*(1), 126-168. [CrossRef]

[16] Dickens, G. R. (2003). Rethinking the global carbon cycle with a large, dynamic and microbially mediated gas hydrate capacitor. *Earth and Planetary Science Letters, 213*(3-4), 169-183. [CrossRef]

[17] Milkov, A. V. (2004). Global estimates of hydrate-bound gas in marine sediments: how much is really out there?. *Earth-science reviews, 66*(3-4), 183-197. [CrossRef]

[18] Collett, T. S. (2002). Energy resource potential of natural gas hydrates. *AAPG bulletin, 86*(11), 1971-1992. [CrossRef]

[19] Makogon, Y. F. (2010). Natural gas hydrates–A promising source of energy. *Journal of natural gas science and engineering, 2*(1), 49-59. [CrossRef]

[20] Xu, C. G., & Li, X. S. (2015). Research progress on methane production from natural gas hydrates. *RSC advances, 5*(67), 54672-54699. [CrossRef]

[21] Maslin, M., Owen, M., Day, S., & Long, D. (2004). Linking continental-slope failures and climate change: Testing the clathrate gun hypothesis. *Geology, 32*(1), 53-56. [CrossRef]

[22] Dickens, G. R., O'Neil, J. R., Rea, D. K., & Owen, R. M. (1995). Dissociation of oceanic methane hydrate as a cause of the carbon isotope excursion at the end of the Paleocene. *Paleoceanography, 10*(6), 965-971. [CrossRef]

[23] Maslin, M., Owen, M., Betts, R., Day, S., Dunkley Jones, T., & Ridgwell, A. (2010). Gas hydrates: past and future geohazard?. *Philosophical Transactions of the Royal Society A: Mathematical, Physical and Engineering Sciences, 368*(1919), 2369-2393. [CrossRef]

[24] Li, Q., Zhao, D., Yin, J., Zhou, X., Li, Y., Chi, P., ... & Cheng, Y. (2023). Sediment Instability Caused by Gas Production from Hydrate-bearing Sediment in Northern South China Sea by Horizontal Wellbore: Evolution and Mechanism. *Natural Resources Research, 32*(4), 1595-1620. [CrossRef]

[25] Rutqvist, J., & Moridis, G. J. (2009). Numerical studies on the geomechanical stability of hydrate-bearing sediments. *Spe Journal, 14*(02), 267-282. [CrossRef]

[26] Klar, A., Soga, K., & Ng, M. Y. A. (2010). Coupled deformation–flow analysis for methane hydrate extraction. *Geotechnique, 60*(10), 765-776. [CrossRef]

[27] Li, Q., Zhang, C., Yang, Y., Ansari, U., Han, Y., Li, X., & Cheng, Y. (2023). Preliminary experimental investigation on long-term fracture conductivity for evaluating the feasibility and efficiency of fracturing operation in offshore hydrate-bearing sediments. *Ocean Engineering, 281*, 114949. [CrossRef]

[28] Kim, J., Moridis, G. J., & Rutqvist, J. (2012). Coupled flow and geomechanical analysis for gas production in the Prudhoe Bay Unit L-106 well Unit C gas hydrate deposit in Alaska. *Journal of petroleum science and engineering, 92*, 143-157. [CrossRef]

[29] Moridis, G. J., & Reagan, M. T. (2007, April). Strategies for gas production from oceanic class 3 hydrate accumulations. In *Offshore technology conference* (pp. OTC-18865). OTC. [CrossRef]

[30] Masui, A., Haneda, H., Ogata, Y., & Aoki, K. (2005, June). Effects of methane hydrate formation on shear

strength of synthetic methane hydrate sediments. In *ISOPE International Ocean and Polar Engineering Conference* (pp. ISOPE-I). Isope.

[31] Hyodo, M., Li, Y., Yoneda, J., Nakata, Y., Yoshimoto, N., Nishimura, A., & Song, Y. (2013). Mechanical behavior of gas-saturated methane hydrate-bearing sediments. *Journal of geophysical research: solid earth, 118*(10), 5185-5194. [CrossRef]

[32] Yoneda, J., Masui, A., Konno, Y., Jin, Y., Egawa, K., Kida, M., ... & Tenma, N. (2015). Mechanical behavior of hydrate-bearing pressure-core sediments visualized under triaxial compression. *Marine and petroleum geology, 66*, 451-459. [CrossRef]

[33] Sun, X., Luo, T., Wang, L., Wang, H., Song, Y., & Li, Y. (2019). Numerical simulation of gas recovery from a low-permeability hydrate reservoir by depressurization. *Applied energy, 250*, 7-18. [CrossRef]

[34] Uchida, S., Soga, K., & Yamamoto, K. (2012). Critical state soil constitutive model for methane hydrate soil. *Journal of geophysical research: solid earth, 117*(B3). [CrossRef]

[35] Sánchez, M., Gai, X., & Santamarina, J. C. (2017). A constitutive mechanical model for gas hydrate bearing sediments incorporating inelastic mechanisms. *Computers and Geotechnics, 84*, 28-46. [CrossRef]

[36] Xue, M., Cheng, Y., Li, Y., Yan, C., Han, Z., Chen, Y., & Sun, B. (2023). Numerical Analysis on Gas Production and Geomechanical Responses of Natural Gas Hydrate Reservoirs. *ACS omega, 8*(42), 39604-39615. [CrossRef]

[37] Jiang, M., Sun, C., Crosta, G. B., & Zhang, W. (2015). A study of submarine steep slope failures triggered by thermal dissociation of methane hydrates using a coupled CFD-DEM approach. *Engineering Geology, 190*, 1-16. [CrossRef]

[38] Ning, F., Yu, Y., Kjelstrup, S., Vlugt, T. J., & Glavatskiy, K. (2012). Mechanical properties of clathrate hydrates: status and perspectives. *Energy & Environmental Science, 5*(5), 6779-6795. [CrossRef]

[39] Waite, W. F., Santamarina, J. C., Cortes, D. D., Dugan, B., Espinoza, D. N., Germaine, J., ... & Yun, T. S. (2009). Physical properties of hydrate-bearing sediments. *Reviews of geophysics, 47*(4). [CrossRef]

[40] Sun, X., Wang, L., Luo, H., Song, Y., & Li, Y. (2019). Numerical modeling for the mechanical behavior of marine gas hydrate-bearing sediments during hydrate production by depressurization. *Journal of Petroleum Science and Engineering, 177*, 971-982. [CrossRef]

[41] Wan, Y., Wu, N., Hu, G., Xin, X., Jin, G., Liu, C., & Chen, Q. (2018). Reservoir stability in the process of natural gas hydrate production by depressurization in the Shenhu area of the South China Sea. *Natural Gas Industry B, 5*(6), 631-643. [CrossRef]

[42] Moridis, G. J., Collett, T. S., Pooladi-Darvish, M., Hancock, S., Santamarina, C., Boswell, R., ... & Koh, C. A. (2011). Challenges, uncertainties, and issues facing gas production from gas-hydrate deposits. *SPE reservoir evaluation & engineering, 14*(01), 76-112. [CrossRef]

[43] Wang, K., Chang, Y., Chen, G., Sun, B., Sun, H., Li, H., & Dai, Y. (2022). Three-dimensional mechanical behaviors of casing during gas production from marine hydrate reservoirs using depressurization. *Energy, 247*, 123526. [CrossRef]

[44] Guo, Z., Wang, H., & Jiang, M. (2021). A simple analytical model of wellbore stability considering methane hydrate saturation-dependent elastoplastic mechanical properties. *Journal of Petroleum Science and Engineering, 207*, 109104. [CrossRef]

[45] He, Y., Song, B., & Li, Q. (2023). Coupling submarine slope stability and wellbore stability analysis with natural gas hydrate drilling and production in submarine slope strata in the South China Sea. *Journal of Marine Science and Engineering, 11*(11), 2069. [CrossRef]

[46] Cheng, Y., Xue, M., Shi, J., Li, Y., Yan, C., Han, Z., & Yang, J. (2023). Numerical simulating the influences of hydrate decomposition on wellhead stability. *Processes, 11*(6), 1586. [CrossRef]

[47] Uchida, T., Takeya, S., Chuvilin, E. M., Ohmura, R., Nagao, J., Yakushev, V. S., ... & Narita, H. (2004). Decomposition of methane hydrates in sand, sandstone, clays, and glass beads. *Journal of Geophysical Research: Solid Earth, 109*(B5). [CrossRef]

[48] Konno, Y., Fujii, T., Sato, A., Akamine, K., Naiki, M., Masuda, Y., ... & Nagao, J. (2017). Key findings of the world's first offshore methane hydrate production test off the coast of Japan: Toward future commercial production. *Energy & Fuels, 31*(3), 2607-2616. [CrossRef]

[49] Liu, C., Meng, Q., He, X., Li, C., Ye, Y., Zhang, G., & Liang, J. (2015). Characterization of natural gas hydrate recovered from Pearl River Mouth basin in South China Sea. *Marine and Petroleum Geology, 61*, 14-21. [CrossRef]

[50] Li, Q., Liu, J., Wang, S., Guo, Y., Han, X., Li, Q., ... & Zhang, X. (2024). Numerical insights into factors affecting collapse behavior of horizontal wellbore in clayey silt hydrate-bearing sediments and the accompanying control strategy. *Ocean Engineering, 297*, 117029. [CrossRef]

[51] Li, G., Moridis, G. J., Zhang, K., & Li, X. S. (2010). Evaluation of gas production potential from marine gas hydrate deposits in Shenhu area of South China Sea. *Energy & Fuels, 24*(11), 6018-6033. [CrossRef]

[52] Su, Z., Cao, Y., Wu, N., Chen, D., Yang, S., & Wang, H. (2012). Numerical investigation on methane hydrate accumulation in Shenhu Area, northern continental slope of South China Sea. *Marine and Petroleum Geology, 38*(1), 158-165. [CrossRef]

[53] Zhang, W., Liang, J., Wei, J., Su, P., Lin, L., & Huang, W. (2019). Origin of natural gases and associated gas

hydrates in the Shenhu area, northern South China Sea: Results from the China gas hydrate drilling expeditions. *Journal of Asian Earth Sciences, 183*, 103953. [CrossRef]

[54] Qin, X. W., Lu, J. A., Lu, H. L., Qiu, H. J., Liang, J. Q., Kang, D. J., ... & Kuang, Z. G. (2020). Coexistence of natural gas hydrate, free gas and water in the gas hydrate system in the Shenhu Area, South China Sea. *China Geology, 3*(2), 210-220. [CrossRef]

[55] Wang, L., Yang, H., Sun, C., Sun, J., Hao, X., Li, C., ... & Chen, Y. (2025). A Comparative Study on the Occurrence and Pore Structure Characteristics of CH4 and CO2 Hydrates in Sandy Sediments Using SEM-EDS Technology. *Gas Science and Engineering*, 205803. [CrossRef]

[56] Priest, J. A., Best, A. I., & Clayton, C. R. (2005). A laboratory investigation into the seismic velocities of methane gas hydrate-bearing sand. *Journal of geophysical research: solid earth, 110*(B4). [CrossRef]

[57] Jang, J., & Santamarina, J. C. (2011). Recoverable gas from hydrate-bearing sediments: Pore network model simulation and macroscale analyses. *Journal of geophysical research: Solid Earth, 116*(B8). [CrossRef]

[58] Qingchao, L., Jingjuan, W., Qiang, L., Fuling, W., & Yuanfang, C. (2025). Sediment Instability Caused by Gas Production from Hydrate-Bearing Sediment in Northern South China Sea by Horizontal Wellbore: Sensitivity Analysis. *Natural Resources Research, 34*(3), 1667-1699. [CrossRef]

[59] Moridis, G. J., Kowalsky, M. B., & Pruess, K. (2007). Depressurization-induced gas production from class 1 hydrate deposits. *SPE Reservoir Evaluation & Engineering, 10*(05), 458-481. [CrossRef]

[60] Song, Y., Zhu, Y., Liu, W., Zhao, J., Li, Y., Chen, Y., ... & Ji, C. (2014). Experimental research on the mechanical properties of methane hydrate-bearing sediments during hydrate dissociation. *Marine and petroleum geology, 51*, 70-78. [CrossRef]

[61] Jang, J., & Santamarina, J. C. (2014). Evolution of gas saturation and relative permeability during gas production from hydrate-bearing sediments: Gas invasion vs. gas nucleation. *Journal of Geophysical Research: Solid Earth, 119*(1), 116-126. [CrossRef]

[62] Dai, S., Santamarina, J. C., Waite, W. F., & Kneafsey, T. J. (2012). Hydrate morphology: Physical properties of sands with patchy hydrate saturation. *Journal of geophysical research: solid earth, 117*(B11). [CrossRef]

[63] Yun, T. S., Santamarina, J. C., & Ruppel, C. (2007). Mechanical properties of sand, silt, and clay containing tetrahydrofuran hydrate. *Journal of geophysical research: solid earth, 112*(B4). [CrossRef]

[64] Ghiassian, H., & Grozic, J. L. (2013). Strength behavior of methane hydrate bearing sand in undrained triaxial testing. *Marine and petroleum geology, 43*, 310-319. [CrossRef]

[65] Zhang, J., Zhang, Y., Wu, N., Li, Y., Chen, Q., Wei, J., ... & Liu, C. (2025). Prediction of mechanical characteristics and micro-mechanism analysis of fracture-filling hydrate-bearing sediments. *Applied Ocean Research, 165*, 104795. [CrossRef]

[66] Wei, N., Zhang, C., Zhou, L., Zhang, S., Zhou, S., Zhang, L., ... & Kvamme, B. (2025). Evolution law of physical parameters and hydrate reservoir productivity under multi-stage depressurization. *Petroleum*. [CrossRef]

[67] Miyazaki, K., Masui, A., Sakamoto, Y., Aoki, K., Tenma, N., & Yamaguchi, T. (2011). Triaxial compressive properties of artificial methane-hydrate-bearing sediment. *Journal of geophysical research: solid earth, 116*(B6). [CrossRef]

[68] Zhang, Z., Liu, L., Ning, F., Liu, Z., Sun, J., Li, X., ... & Liu, C. (2022). Effect of stress on permeability of clay silty cores recovered from the Shenhu hydrate area of the South China Sea. *Journal of Natural Gas Science and Engineering, 99*, 104421. [CrossRef]

[69] Minagawa, H., Nishikawa, Y., Ikeda, I., Miyazaki, K., Takahara, N., Sakamoto, Y., ... & Narita, H. (2008). Characterization of sand sediment by pore size distribution and permeability using proton nuclear magnetic resonance measurement. *Journal of Geophysical Research: Solid Earth, 113*(B7). [CrossRef]

[70] Guo, X., Jin, Y., Miu, T., Wei, S., Xia, Y., & Tang, J. (2026). Investigation of the time-dependent and dynamic geomechanical behaviors induced by depressurization in natural gas hydrate-bearing sediments based on a poro-elasto-viscoplastic-dynamic model. *International Journal of Rock Mechanics and Mining Sciences, 197*, 106357. [CrossRef]

[71] Li, M., Liu, J., & Xia, Y. (2025). Risk prediction of gas hydrate formation in the wellbore and subsea gathering system of deep-water turbidite reservoirs: Case analysis from the south China Sea. *Reservoir Science, 1*(1), 52-72. [CrossRef]

[72] Li, Y. B., Xin, X., Zhu, H. X., Su, Y., Yuan, Y. L., & Xu, T. F. (2025). Research progress and scientific challenges in permeability evolution of hydrate bearing sediments. *Petroleum Science*. [CrossRef]

[73] Wang, H., Feng, F., Zhang, J., Han, X., Zhang, Y., & Zhang, K. (2024). Impact of rock strength degradation by fluid intrusion on borehole stability in shale. *Natural Gas Industry B, 11*(5), 553-568. [CrossRef]

[74] Liu, Y., Li, Y., Zhang, Z., Li, G., Hou, J., Ma, C., ... & Chen, Z. (2025). Study on stress sensitivity of clayey silt hydrate-bearing sediments and its influence law on production. *Water Research*, 124620. [CrossRef]

[75] Rutqvist, J., Moridis, G. J., Grover, T., Silpngarmlert, S., Collett, T. S., & Holdich, S. A. (2012). Coupled multiphase fluid flow and wellbore stability analysis associated with gas production from oceanic hydrate-bearing sediments. *Journal of petroleum science and engineering, 92*, 65-81. [CrossRef]

[76] Wu, N., Zhang, H., Yang, S., Zhang, G., Liang, J., Lu, J. A., ... & Zhu, Y. (2011). Gas hydrate system of Shenhu area, northern South China Sea: geochemical results. *Journal of Geological Research, 2011*(1), 370298. [CrossRef]

[77] Wang, X., Lee, M., Collett, T., Yang, S., Guo, Y., & Wu, S. (2014). Gas hydrate identified in sand-rich inferred sedimentary section using downhole logging and seismic data in Shenhu area, South China Sea. *Marine and Petroleum Geology, 51*, 298-306. [CrossRef]

[78] Uchida, S., Seol, Y., & Yamamoto, K. (2019). Geomechanical behavior of gas hydrate-bearing reservoir during gas production. In *Proceedings of the AAPG Asia Pacific Region Geosciences Technology Workshop*. [CrossRef]

[79] Li, X., Sun, B., Li, H., Liu, H., Cai, D., Wang, X., & Li, X. (2024). Simulation of gas production and seafloor subsidence during the development of natural gas hydrates in the south china sea. *Energy & Fuels, 38*(10), 8674-8687. [CrossRef]

[80] Dong, L., Wu, N., Leonenko, Y., Wan, Y., Liao, H., Hu, G., & Li, Y. (2023). A coupled thermal-hydraulic-mechanical model for drilling fluid invasion into hydrate-bearing sediments. *Energy, 278*, 127785. [CrossRef]

[81] Gong, B., Jiang, Y., Yan, P., & Zhang, S. (2020). Discrete element numerical simulation of mechanical properties of methane hydrate-bearing specimen considering deposit angles. *Journal of Natural Gas Science and Engineering, 76*, 103182. [CrossRef]

[82] Huang, L., Xu, C., Xu, J., & Zhao, Y. (2022). Hydrate dissociation evaluation and stratum subsidence response induced by depressurization in hydrate-bearing permafrost. *Energy & Fuels, 36*(18), 11077-11088. [CrossRef]

[83] Ji, Y., Hou, J., Zhao, E., Liu, C., Guo, T., Liu, Y., ... & Bai, Y. (2021). Pore-scale study on methane hydrate formation and dissociation in a heterogeneous micromodel. *Journal of Natural Gas Science and Engineering, 95*, 104230. [CrossRef]

[84] Jin, G., Lei, H., Xu, T., Liu, L., Xin, X., Zhai, H., & Liu, C. (2019). Seafloor subsidence induced by gas recovery from a hydrate-bearing sediment using multiple well system. *Marine and Petroleum Geology, 107*, 438-450. [CrossRef]

[85] Wang, X., Wu, S., Lee, M., Guo, Y., Yang, S., & Liang, J. (2011). Gas hydrate saturation from acoustic impedance and resistivity logs in the Shenhu area, South China Sea. *Marine and Petroleum Geology, 28*(9), 1625-1633. [CrossRef]

[86] Wan, Y., Wu, N., Chen, Q., Li, W., Hu, G., Huang, L., & Ouyang, W. (2022). Coupled thermal-hydrodynamic-mechanical–chemical numerical simulation for gas production from hydrate-bearing sediments based on hybrid finite volume and finite element method. *Computers and Geotechnics, 145*, 104692. [CrossRef]

[87] Wang, Z., Zhang, Y., Peng, Z., Shan, Z., Sun, B., & Sun, J. (2022). Recent advances in methods of gas recovery from hydrate-bearing sediments: A Review. *Energy & Fuels, 36*(11), 5550-5593. [CrossRef]

[88] Yan, C., Cheng, Y., Li, M., Han, Z., Zhang, H., Li, Q., ... & Ding, J. (2017). Mechanical experiments and constitutive model of natural gas hydrate reservoirs. *International Journal of Hydrogen Energy, 42*(31), 19810-19818. [CrossRef]

[89] Yang, Q., Xu, J., Ren, Y., Han, Y., Zhou, C., Yang, G., ... & Yu, L. (2025). Key mechanical properties of hydrate bearing sediment: state of the art and prospects. *Geoenergy Science and Engineering*, 214079. [CrossRef]

[90] Su, M., Wang, H., Sha, Z., Liang, J., Wu, N., Qiao, S., ... & Yang, R. J. G. A. (2016). Gas hydrates distribution in the Shenhu Area, northern South China Sea: comparisons between the eight drilling sites with gas-hydrate petroleum system. *Geologica Acta, 14*(2), 0079-100. [CrossRef]

[91] Li, Q., Li, Q., Wu, J., He, K., Xia, Y., Liu, J., ... & Cheng, Y. (2025). Wellhead Stability During Development Process of Hydrate Reservoir in the Northern South China Sea: Sensitivity Analysis. *Processes, 13*(6), 1630. [CrossRef]

[92] Li, Q., Li, Q., Wu, J., Li, X., Li, H., & Cheng, Y. (2024). Wellhead stability during development process of hydrate reservoir in the Northern South China Sea: Evolution and mechanism. *Processes, 13*(1), 40. [CrossRef]

[93] Yoon, H. C., Yoon, S., Lee, J. Y., & Kim, J. (2021). Multiple porosity model of a heterogeneous layered gas hydrate deposit in Ulleung Basin, East Sea, Korea: A study on depressurization strategies, reservoir geomechanical response, and wellbore stability. *Journal of Natural Gas Science and Engineering, 96*, 104321. [CrossRef]

[94] Wang, L., Liu, Z., Yan, X., Wu, Z., Liu, Z., Ma, S., & Li, Y. (2025). Stress-strain and creep behaviors of marine overconsolidated hydrate-bearing sediments. *Geoenergy Science and Engineering, 254*, 214036. [CrossRef]

[95] Chen, H. E., Shan, W., & Ma, Y. (2025). Permeability characteristics of hydrate-bearing sediments during hydrate formation and depressurization decomposition processes. *Geoenergy Science and Engineering*, 214099. [CrossRef]

[96] Li, S., Ding, S., Wu, D., Wang, X., Hao, Y., Li, Q., & Pang, W. (2021). Analysis of stratum subsidence induced by depressurization at an offshore hydrate-bearing sediment. *Energy & Fuels, 35*(2), 1381-1388. [CrossRef]

[97] Sun, H., Chang, Y., Sun, B., Wang, K., Chen, G., Li, H., & Dai, Y. (2023). Spatial-temporal evolution of reservoir effective stress during marine hydrate

depressurization production. *International Journal of Hydrogen Energy, 48*(86), 33483-33495. [CrossRef]

[98] Chen, P., Xu, J., Fan, Q., Zhu, Z., Feng, S., Zhou, Y., ... & Wei, C. (2025). Shear strength behavior of hydrate-bearing sediments under varying dissociation conditions. *Journal of Rock Mechanics and Geotechnical Engineering, 17*(6), 3819-3832. [CrossRef]

[99] Yamamoto, K., Kanno, T., Wang, X. X., Tamaki, M., Fujii, T., Chee, S. S., ... & Shako, V. (2017). Thermal responses of a gas hydrate-bearing sediment to a depressurization operation. *RSC advances, 7*(10), 5554-5577. [CrossRef]

[100] Shang, Y., Lei, G., Tang, J., Qu, J., & Ning, F. (2025). Permeability of marine gas hydrate-bearing sediments considering effective stress and particle size distribution: A theoretical model. *Computers and Geotechnics, 185*, 107367. [CrossRef]

[101] Sang, S., Kong, L., Zhao, Y., Liu, J., & Hua, L. (2025). Mechanical characterization of hydrate-bearing clayey-silty sediments with layered sediment distribution: Effects of hydrate saturation and effective confining pressure. *Ocean Engineering, 326*, 120879. [CrossRef]

[102] Zhao, Y., Liu, Z., Li, Y., Dou, X., Gong, G., Wu, Q., ... & Ning, F. (2024). Subsidence Characteristics of Hydrate-Bearing Sediments during Depressurization: Insights from Experimental and Discrete Element Method Simulations. *Energy & Fuels, 38*(17), 16202-16217. [CrossRef]

[103] Li, Y., Xin, X., Liu, M., Seol, Y., Xia, Y., Zhu, H., ... & Xu, T. (2025). An experimental study on gas-liquid phase fluid migration in hydrate-bearing sediments during hydrate dissociation. *Engineering Geology, 354*, 108163. [CrossRef]

[104] Yao, Y., Niu, M., Zi, M., Sun, Y. F., & Chen, D. (2025). Coupling depressurization and flue gas flooding to enhance CH4 recovery and CO2 sequestration in hydrate-bearing sediments: Pilot-scale experimental evaluation at marine conditions. *Energy, 333*, 137328. [CrossRef]

[105] Kimoto, S., Oka, F., Fushita, T., & Fujiwaki, M. (2007). A chemo-thermo-mechanically coupled numerical simulation of the subsurface ground deformations due to methane hydrate dissociation. *Computers and geotechnics, 34*(4), 216-228. [CrossRef]

Yanli Wang obtained a Master's degree in Oil and Gas Well Engineering in June 2007. After she got the Master's degree, she was appointed as a senior lecturer at Shandong Institute of Petroleum and Chemical Technology. She has participated in subprojects of the National Science and Technology Major Special Project, including "Research on the Utilization Limits of Different Injection Media in Typical Ultra-Low-Permeability Reservoirs." Meanwhile, In addition, she has authored and co-authored multiple peer-reviewed journal articles, contributing to the advancement of efficient unconventional oil and gas development. (Email: 395497954@qq.com)

Yuanwei Sun obtained Master's degree in Oil and Gas Well Engineering in 2015, he was appointed as a teaching assistant at Shandong Institute of Petroleum and Chemical Technology from then on. At present, his investigation primarily focuses on the fundamental mechanical properties of oil and gas reservoirs and its application of in wellbore stability and hydraulic fracturing. He has led and participated in more than 30 scientific projects, including "Optimization Design of Repetitive Fracturing in the Binnan Low-Permeability Block Based on Geological–Engineering Integration" and "Time-Dependent Study of Long-Term Fracture Conductivity in Well Niuye 1." To date, more than 30 academic papers have been published, including 4 SCI-indexed papers. (Email: 2015004@sdipct.edu.cn)